

Journal of

www.biophotonics-journal.org

BIOPHOTONICS

WILEY-VCH

REPRINT

REVIEW ARTICLE

Quantitative phase imaging for medical diagnosis

Hassaan Majeed¹, Shamira Sridharan², Mustafa Mir³, Lihong Ma⁴, Eunjung Min⁵,
Woonggyu Jung^{5,6}, and Gabriel Popescu*,¹

¹ Quantitative Light Imaging Lab, Beckman Institute for Advanced Science and Technology, University of Illinois at Urbana Champaign, 405 N. Mathews Ave., Urbana, IL, 61801, USA

² Biomedical Engineering Department, University of California Davis, Genome and Biomedical Sciences Facility #2603B, 451 Health Science Dr., Davis, CA, 95616, USA

³ Molecular and Cell Biology, University of California, Berkeley, 485 Li Ka Shing Center, 94720, Berkeley, CA, USA

⁴ Institute of Information Optics, Zhejiang Normal University, Jinhua 321004, China

⁵ Department of Biomedical Engineering, Ulsan National Institute of Science and Technology, 50 UNIST-gil, Ulsan 44919, Republic of Korea

⁶ Center for Soft and Living Matter, Institute for Basic Science (IBS), 50 UNIST-gil, Ulsan 44919, Republic of Korea

Received 30 April 2016, revised 6 July 2016, accepted 13 July 2016

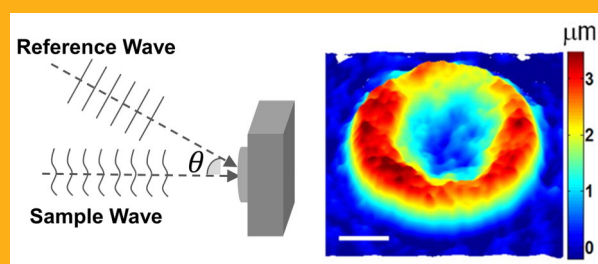
Published online 20 August 2016

Key words: quantitative phase imaging, microscopy, label free imaging, interferometry, pathology, cancer diagnosis, hematological disorders

Optical microscopy is an indispensable diagnostic tool in modern healthcare. As a prime example, pathologists rely exclusively on light microscopy to investigate tissue morphology in order to make a diagnosis. While advances in light microscopy and contrast markers allow pathologists to visualize cells and tissues in unprecedented detail, the interpretation of these images remains largely subjective, leading to inter- and intra-observer discrepancy. Furthermore, conventional microscopy images capture qualitative information which makes it difficult to automate the process, reducing the throughput achievable in the diagnostic workflow. Quantitative Phase Imaging (QPI) techniques have been advanced in recent years to address these two challenges. By quantifying physical parameters of cells and tissues, these systems remove subjectivity from the disease diagnosis process and allow for easier automation to increase throughput. In addition to providing quantitative information, QPI systems are also label-free and can be easily assimilated into the current diagnostic workflow

in the clinic. In this paper we review the advances made in disease diagnosis by QPI techniques. We focus on the areas of hematological diagnosis and cancer pathology, which are the areas where most significant advances have been made to date.

[Image adapted from Y. Park, M. Diez-Silva, G. Popescu, G. Lykotrafitis, W. Choi, M. S. Feld, and S. Suresh, Proc. Natl. Acad. Sci. **105**, 13730–13735 (2008).]



1. Introduction

Quantitative Phase Imaging (QPI) has undergone tremendous progress, especially in the past decade.

In QPI the optical path length shift introduced by the specimen of interest is quantified at each point in the field of view. As a result, QPI yields quantitative information about the structure of the specimen,

* Corresponding author: e-mail: gpopescu@illinois.edu, Tel.: +1-217-333-4840

with nanoscale sensitivity, without the need for staining or tagging. Experimentally one has access to the phase of the correlation function and not that of the field itself [1]. In practical terms, this means that we only measure phase differences, say between a sample and a reference field. The interferometric geometry always involved in QPI grants this approach extreme sensitivity to tissue architecture of 1 nm or less [2]. QPI can be achieved by various approaches, which proliferated the literature with a large number of acronyms, sometimes creating confusions. Those methods successfully applied to clinical problems will be presented with clear nomenclature below.

The label-free operation, nanoscale sensitivity, and quantitative information granted QPI immediate unique applications in live cell imaging. Thus membrane fluctuations of Red Blood Cells (RBCs) were measured with unprecedented sensitivity and interesting new biophysics was unraveled [3–5]. The quantitative nature of the phase map allows us to convert it to dry mass density of the cell with extremely high accuracy of the order of femtograms per squared microns [6–8]. As a result, QPI is a powerful method for studying cell growth. The label-free operation means that the cells can be imaged for a long time, without the restrictions of photobleaching and phototoxicity associated with fluorescence.

A quantitative phase image of an optically thin specimen can be numerically processed and expressed in the spatial frequency domain, which is entirely equivalent to measuring angular scattering from that object. This approach is called Fourier transform light scattering (FTLS), as it represents the spatial analog of Fourier Transform infrared spectroscopy (FTIR) [9]. The equivalence between QPI and light scattering measurements is fundamental to performing tomographic reconstructions of transparent objects. Thus, collecting QPI data along an additional dimension (e.g angle, optical spectrum, z -axis) one can solve a scattering inverse problem and obtain the refractive index distribution of the specimen of interest [10–12].

Building on the existing success of the QPI basic studies, more recently researchers have applied the same approach to various problems of clinical relevance, their research encompassing various diseases [13–16]. QPI has been demonstrated so far as a valuable tool in hematology. The absence of staining means that a few steps in tissue preparation can be skipped and that, with it, the turnaround time and cost can be reduced. Perhaps most interestingly, the quantitative information about biopsied tissue structure allows diagnosis that is objective and independent of observer or preparation bias. This feature also means that QPI data can be compared across instruments and geographical sites, without concerns

regarding color or stain corrections. As biomedicine is clearly becoming a more quantitative and engineering-based field, it is likely that QPI will play an increasingly important role in generating quantitative clinical data.

In this article, we review what appear to be some of the most notable recent developments in clinical QPI. The manuscript is structured as follows. In Section 2 we describe the physical quantities measured by QPI to lay the groundwork for understanding its significance in clinical applications. Section 3 reviews the studies of clinical relevance carried out in the field of diagnostic hematology, using QPI. Section 4 discusses advancements in cancer diagnosis using QPI while Section 5 summarizes this review and makes some concluding remarks. We also include a Supporting Information section which explains some key concepts in QPI, understanding which is important in order to follow the details of the clinical studies we discuss in this review [17].

2. Phase and dry mass

The interaction of light with transparent specimen (such as cells and tissues) involves a change in the phase of the electromagnetic field with respect to some reference. This phase shift is proportional to the integral, along the light propagation direction, of the difference between the refractive index of the specimen and the surrounding medium. Denoting the light propagation direction as the z -axis, the phase map $\phi(x, y)$ is given by

$$\phi(x, y) = \frac{2\pi}{\lambda} \int_0^{h(x,y)} [n_s(x, y, z) - n_m] dz, \quad (1)$$

where $n_s(x, y, z)$ is the refractive index of the specimen as function of space, n_m is the refractive index of the surrounding medium, λ is the wavelength of the illumination source and the integration limits span the thickness of the specimen $h(x, y)$ [2].

Over the years, a number of studies have shown that the refractive index of a cell, $n_{\text{cell}}(x, y)$, has a strong dependence on its total protein concentration $C(x, y)$. This relationship is given by

$$n_{\text{cell}}(x, y) = n_{\text{sol}} + \alpha C(x, y), \quad (2)$$

where n_{sol} is the refractive index of the cytoplasmic solvent and proportionality constant α is called the refractive increment [6, 18, 19]. Since for most applications the difference between the refractive index of the cytoplasmic solvent and the cell immersion media is negligible ($n_m \approx n_{\text{sol}}$) it can be shown that

the cell dry mass density $\rho(x, y)$ is proportional to the phase map $\phi(x, y)$ as [6, 7].

$$\rho(x, y) = \frac{\lambda}{2\pi\alpha} \phi(x, y). \quad (3)$$

These remarkable results have motivated several studies on cell-cycle dependent growth, dynamics of intracellular transport as well as chemical composition of cells through measurement of $\rho(x, y)$ and $C(x, y)$ using QPI [7, 8, 16, 20–22].

It is important to note that QPI methods employing incoherent illumination (white light) differ from those employing coherent illumination (laser light) in important ways, having implications for clinical studies. Incoherent illumination leads to optical sectioning due to temporal coherence gating, meaning that for a thick sample, the integration of phase is over a fraction of its depth. 3D reconstruction of the sample image is thus a possibility by scanning the sample in the z -direction and resolving depth through deconvolution methods [12, 23]. In coherent imaging modalities on the other hand, the integration of phase is over the entire sample depth, making such methods unsuitable for resolving sample structure in the z -direction.

3. Hematological diagnosis using QPI

3.1 Diagnosis from blood testing

Blood is a life-sustaining fluid which carries oxygen and nutrients to the tissues and waste products to the lungs, liver and kidneys. Whole blood has two major components: plasma and formed elements, at concentrations of approximately 55% and 45% respectively. 99% of the formed elements are erythrocytes or Red Blood Cells (RBCs), about 1% are leukocytes or White Blood Cells (WBCs) and less than 1% are platelets [24, 25]. While RBCs participate predominantly in the oxygenation process, WBCs can appear as one of several distinct cell types, each of which performs a unique function.

Blood analysis thus provides a wealth of information about the health of an individual. Analysis of blood helps healthcare professionals determine the physiological state of various organs as well as allowing them to diagnose a myriad of diseases [26]. The chemical composition, morphology, and numbers of various blood cells not only inform on hematological disorders but also reflect non-hematological pathologies of inflammatory, degenerative or neoplastic nature [27]. Hematological disorders alone are widely prevalent and exert significant costs on a country's health infrastructure. The disease statistics for major hematological disorders bear out the scale of the

problem: According to a National Heart, Lung, and Blood Institute (NHLBI) report around 10,000 Americans died due to these disorders in 2010. According the same report, the total direct expenditure due to anemia was \$5 billion in the US for 2010 [28]. The Center of Disease Prevention and Control (CDC) reports that the prevalence of sickle cell disease in the US was 15.5 cases per 1000 births in 2010 [29]. Globally, Malaria is a major public health problem with 198 million reported cases in 2013 according to the World Health Organization (WHO) [30]. Rapid, accurate and cost effective methods of diagnosis are critical in mitigating the burden of these diseases. This urgent need for diagnostic technologies has led to a myriad of technologies being developed for point of care blood testing.

3.2 Current clinical workflow

The standard method for diagnosing blood disorders in a pathology lab has two steps. First, a Complete Blood Count (CBC) is performed using an automated blood analyzer. Modern automated blood analysis instruments include impedance analyzers and flow cytometers. While being very effective in terms of throughput, these instruments offer limited information [27, 31]. For example, while these instruments have the ability measure erythrocyte volume and hemoglobin (Hb) concentrations, they are unable to measure erythrocytic morphologic abnormalities and variations in cell shape [26]. The quantitative indices obtained from these instruments are simply indicators of the overall cell distributions and are unable to characterize poikilocytosis and subtle changes in RBCs and WBCs. These automated counters are primarily designed to produce accurate measurements of normal blood and to alert the technician with “flags” when numerical abnormalities exist. When such flags are raised, as a second step, a microscopic examination of the peripheral blood smear is required in order to obtain sufficient information on cellular morphology for reaching a diagnosis [27, 31]. In some cases other supplementary tests may also be required. Even though automated blood analyzers have reduced the number of samples that require smears to 15%, the examination of a smear is still an indispensable tool in providing differential diagnosis (commonly for anemias and thrombocytopenia), recommending further tests, speedy diagnosis of certain infections and the identification of leukemia and lymphoma [26, 32].

To prepare a peripheral blood smear for examination, the blood cells are preserved by adding methanol, a process known as fixation. The fixed film of blood is stained with a mixture of several dyes so that the individual cells can be recognized

when they are examined with a microscope [27, 31]. After staining, the color of red cells is enhanced and the white cells and platelets, which would otherwise be transparent and colorless, have acquired a variety of colors which allow their detailed structure to be recognized. The staining process accounts for more than 80% of the time and cost in smear preparation. For maximal information to be derived from a blood smear, the examination must be performed by an experienced and skilled person, either a laboratory scientist or a medically qualified hematologist or pathologist [26, 33]. This examination has the same limitations that all qualitative microscopy based methods have: low throughput and observer subjectivity.

Quantitative Phase Imaging (QPI) technologies have the potential to overcome these limitations in the current clinical workflow. Since QPI techniques image cells label-free, both the time and resources devoted to staining are spared. Furthermore, by providing quantitative maps of cells at microscopic resolution, these technologies have the potential to replace the standard two-step process with a single step automated microscopic analysis. The optical path length maps generated by these techniques can be used to quantify 3D morphology of cells in blood, measure their non-liquid content (dry mass), their mechanical properties and their scattering properties, all of which are discussed in the following sections.

3.3 QPI for RBC screening

3.3.1 Introduction

Most of the blood analysis done using QPI techniques has been geared toward RBCs. Mature erythrocytes represent a very particular type of structure; they lack nuclei and organelles and thus can be modeled as optically homogeneous objects. Since RBCs comprise mainly of Hb, from Eq. (2) the cell refractive index n_{RBC} can be expressed as

$$n_{\text{RBC}} = n_{\text{sol}} + \alpha(\text{MCHC}), \quad (4)$$

where MCHC refers to the Mean Corpuscular Hb Concentration and n_{sol} is the refractive index of the cytoplasmic solvent [20, 34, 35]. Because the RBC cytoplasm is chemically homogenous, the cell refractive index can be described as being spatially invariant. From Eq. (1), this means that the phase ϕ of an RBC is proportional to its thickness and can be used to extract a thickness or height map of the cell as

$$h(x, y) = \frac{\lambda}{2\pi(n_{\text{RBC}} - n_m)} \phi(x, y) \quad (5)$$

Therefore, measuring quantitative phase images of red blood cells provides cell thickness maps with an accuracy that corresponds to a very small fraction of the optical wavelength [2, 36]. This means that from QPI measurements the 3D morphology of a cell can be characterized, as described in Section 3.3.2. Furthermore, as discussed in Section 3.3.3, the information available in QPI images can be leveraged to obtain the MCHC or chemical composition of an RBC. As discussed in Section 3.3.4, the RBC thickness maps can be used to probe the dynamics of the cell membrane which can inform on its mechanical properties. Finally, since QPI measurements allow simultaneous extraction of both amplitude and phase of the image field, they can be used to obtain the scattering parameters of RBCs (Section 3.3.5).

In short, QPI can be used to characterize 3D morphology, Hb concentration and mechanical scattering properties of RBCs each of which provide crucial information on cell and patient health. QPI thus offers a powerful new blood screening utility that can be used to aid in making differential diagnosis by an experienced pathologist. QPI instruments can be simply added on as a modality to any existing microscopy, and no special sample preparation is necessary to integrate it into the clinical workflow. Recently real-time QPI based blood analysis has also been demonstrated, further demonstrating the abilities of this technology to be deployed as a point of care tool [37]. Advancements in spectroscopic measurements, image processing and computing power will continue to augment the abilities of QPI presented in this review, while maintaining its position as a low cost, high throughput and highly sensitive instrument.

3.3.2 RBC morphology

Abnormalities in RBC morphology can be indicative of a number of pathologies – some symptoms of more serious conditions and other disorders on their own. Cell geometry alone is a useful marker for patient health: Macrocytosis (enlarged cells) can indicate macrocytic anemia, spherocytosis (spherical cells) can indicate hemolytic anemia and anisocytosis (unequal size distribution) is one of the symptoms of thalassemia major [24, 26, 31]. Other diseases such as sickle cell anemia and malaria too affect cell morphology in ways that are important to quantify accurately and in a timely manner [38–41].

QPI methods have been extensively used to quantify RBC morphological parameters. In the simplest techniques it has been assumed that since RBCs have a homogenous cytoplasm, they can be described as having a spatially invariant refractive

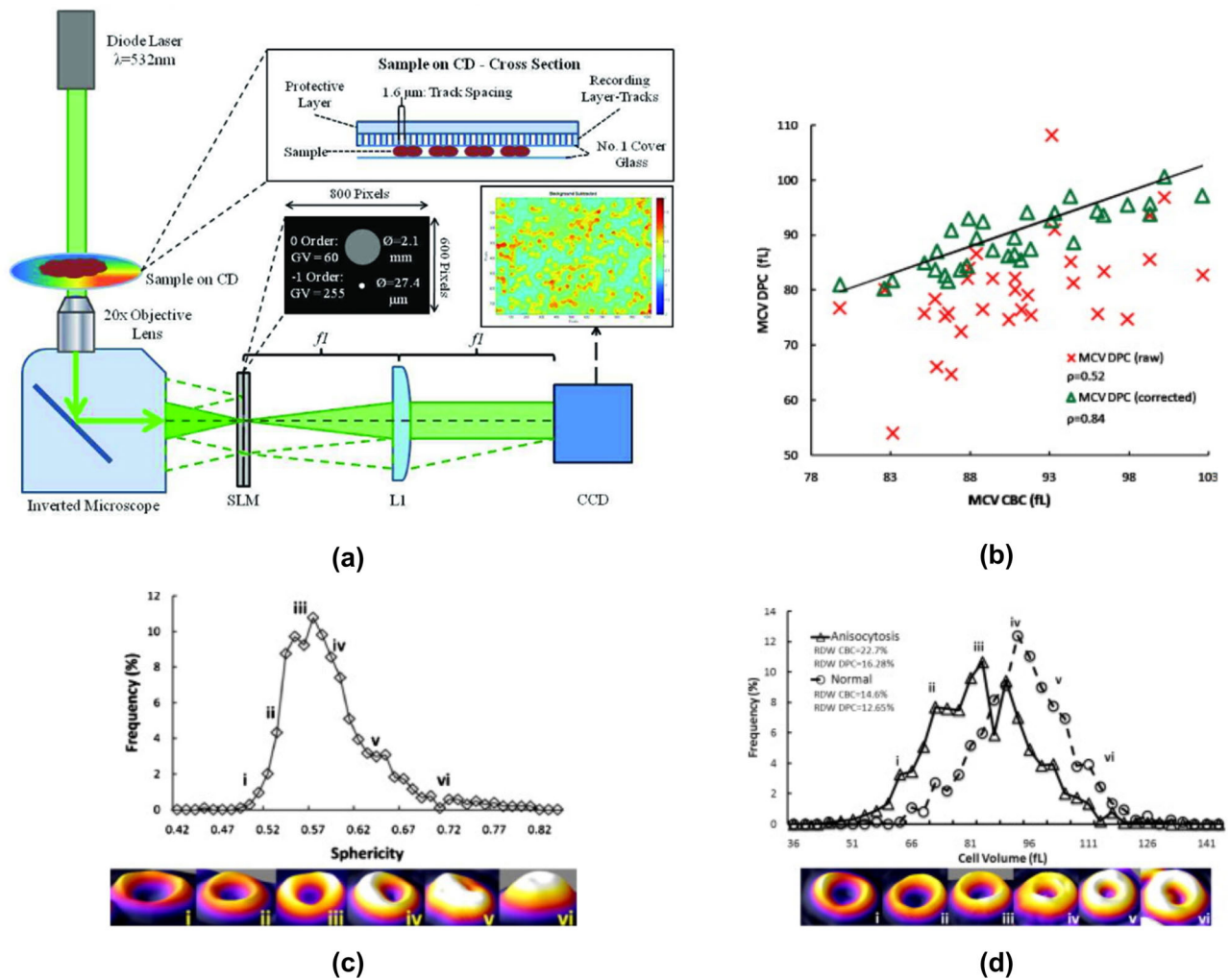


Figure 1 (a) The optical setup of Diffraction Phase Cytometry (DPC). Adapted with permission from Ref. [43]. (b) MCV as measured by DPC (points) and CBC results from an impedance analyzer (solid line). Red points show the MCV calculated with same MCHC for each cell while green points show MCV with individual cell MCHC (obtained from CBC) factored in. Pearson correlation coefficients ρ between CBC and DPC data are shown (c) Histogram of sphericity measured using DPC for cells of a patient suffering from anisocytosis. Images of cells at sphericity values i. 0.50, ii. 0.54, iii. 0.57, iv. 0.61, v. 0.65 and vi. 0.72 are shown. (d) Histograms of Cell Volume for normal individual as well as an individual with anisocytosis. RDW values are markedly different between the two individuals according to both CBC and DPC. Adapted with permission from Ref. [42].

index. As discussed earlier, according to Eq. (5), this assumption allows one to extract the thickness map which then allows computation of 3D cell morphology. Figure 1 shows the results obtained using this approach by a technique called Diffraction Phase Cytometry (DPC) [42].

DPC is an off-axis, common-path, laser-based method, characterized by high-acquisition rate and temporal sensitivity. The optical setup for DPC is illustrated in Figure 1a. Designed with the intention of deploying in resource poor settings, DPC comprises of a standard Compact Disc (CD) that functions as a diffraction grating [43]. The specimen of interest is placed on the CD which is illuminated by

a coherent laser source. The laser light is split by the grating into two identical orders. As shown, the first order is used to generate a plane wave reference U_r by spatially low pass filtering it via a pinhole placed in a conjugate Fourier plane. As shown, the filter can be conveniently generated by using a spatial light modulator (SLM) in amplitude mode. The zeroth order, on the other hand, goes through unaffected and is imaged onto the camera plane by lens L1 to form the sample field $U_s(x, y)$. Interference between U_r and $U_s(x, y)$ generates an intensity image (given by Eq. (1.1) in the Supporting Information section) from which $\phi(x, y)$ can be extracted by using the standard off-axis reconstruction methods

discussed in Section 1 of the Supporting Information section [17].

Three crucial morphological parameters, Mean Corpuscular Volume (MCV), sphericity and Red cell Distribution Width (RDW), were obtained from thickness maps extracted from DPC images. MCV and RDW for the cell population were compared with values reported for the same population by a CBC while the same comparison for sphericity was not possible since this parameter is not reported in a CBC. The comparison showed reasonable agreement between the CBC and DPC results once the MCHC of each cell had been factored in the calculation of cell refractive index (Eq. (4)). The MCHC used for each cell was the value reported for the population it belonged to by the CBC. The results showed that if MCHC can be measured for the cells,

values similar to a CBC are obtainable using DPC with the advantage of increased resolution since the latter is a microscopy technique. The MCHC can be measured in QPI modalities by methods described in Section 3.3.3. In contrast with CBC, DPC was also able to measure additional parameters (such as sphericity) which in the normal diagnostic workflow would have to be assessed by a follow up blood smear microscopic examination. The results showed that QPI had the potential of altering this diagnostic workflow so that only a single microscopic examination maybe required to provide information currently obtained in two steps [42, 43].

More complex QPI systems have employed tomographic image reconstruction to generate 3D refractive index maps of RBCs allowing for simultaneous measurement of 3D morphology and Hb con-

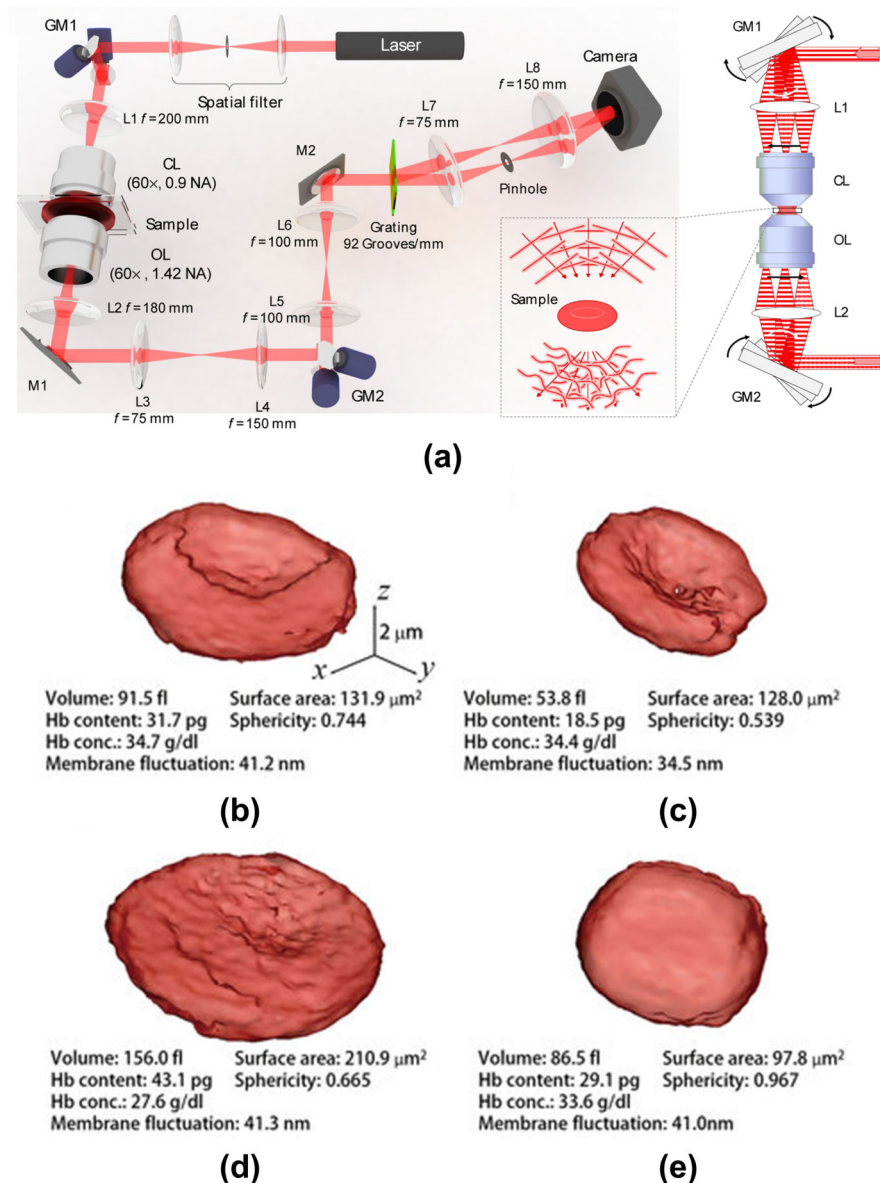


Figure 2 (a) Optical setup of Common-path Diffraction Optical Tomography (cDOT) where Diffraction Phase Microscopy (DPM) is combined with Diffraction Tomography (DT) to carry out 3D phase reconstruction of RBCs. Adapted with permission from Ref. [10]. (b–e) Isosurfaces and morphological parameters extracted from the 3D refractive index maps obtained using cDOT. Comparison in terms of 3D morphology, Hb concentration and membrane dynamics of RBC is shown between (b) healthy individual and patients with (c) iron deficiency anemia (IDA) (d) reticulocytosis and (e) hereditary spherocytosis (HS). Adapted with permission from Ref. [44].

tent (Eqs. (4–5)). Figure 2 shows the results obtained from such a study using a QPI method called Common-path Diffraction Optical Tomography (cDOT) which operates by combining Diffraction Tomography (DT) with Diffraction Phase Microscopy (DPM) [10, 44]. The optical setup of cDOT is illustrated in Figure 2a and b.

DPM is an off-axis, common-path and laser-based QPI technique which operates on essentially the same principle as DPC and, hence, uses the same off-axis phase reconstruction method. The only difference is that the diffraction grating in DPM is placed in a conjugate image plane as opposed to the sample plane itself. Since its invention in 2006, DPM has been widely used as a stable and high-throughput method for extracting the complex image field associated with an object and, therefore, its phase [45, 46]. cDOT uses the DPM configuration to measure the complex image field of an RBC at several illumination angles. As shown, the angular scanning of the illumination is carried out by using two synchronized galvanometric mirrors GM1 and GM2. After extracting the complex image field at each illumination angle through DPM processing, an Optical Diffraction Tomography (ODT) algorithm (described in detail elsewhere in Refs. [47, 48]) is used for reconstruction of the 3D refractive index map of each RBC.

Figure 2b–e compare the 3D morphology (through geometrical parameters) for cells in different pathological states, measured using cDOT. Once again, cDOT measures parameters such as surface area and sphericity that are not available in a CBC and can only be assessed qualitatively in a blood smear examination [44]. In another study, the cDOT system has also been employed to study the 3D morphological changes incurred by mouse RBCs (in terms of volume, surface area and sphericity changes) due to infection by protozoan parasite *Babesia microti*. The parasite causes babesiosis in humans and this study using QPI used a mouse model to elucidate phenomena that are relevant for diagnosis and treatment of the disease in humans [49].

Other researchers have incorporated optical tweezers into QPI systems to capture images of RBCs from several viewing angles which can then be used to map the 3D morphology of the cell [50, 51]. Imaging the RBC at multiple angles allows the decoupling of the refractive index and cell thickness information (see Section 3.3.3). With the thickness information $h(x, y)$ available at various viewing angles, reconstruction algorithms (e.g. shape from silhouette (SFS) algorithm used in Refs. [50] and [52]) can be employed to map the 3D RBC morphology.

In other examples, morphology of RBCs from sickle cell trait patients (Ref. [53]), of RBCs in umbilical cord blood of new-born infants (Ref. [54]) and

of RBCs in storage for transfusion purposes (Refs. [55] and [56]) has also been measured using QPI for comparison with controls. By giving access to detailed 2D and 3D morphological parameters such as volume, surface area, sphericity, diameter, etc., QPI provides new information that is currently unavailable from commercial instruments. It is known that the distributions of these parameters and correlations between them reveal physiologically important information about a given blood sample. QPI, therefore, has the potential to be both a powerful diagnostic tool and a way to improve blood testing efficiency by reducing the number of cases that require a manual smear analysis.

3.3.3 RBC Hb content

The Hb content of RBCs is generally described by two parameters: Mean Corpuscular Hemoglobin (MCH) representing average mass of Hb per cell and Mean Corpuscular Hemoglobin Concentration (MCHC) representing the average cellular concentration of Hb in a cell population. Abnormal values of MCH and MCHC are indicative of pathologies such as hyper- and hypochromic anemias [24]. QPI techniques can be used to assay Hb content and therefore provide diagnostically relevant information about these disorders. As shown by Eq. (4) the cell refractive index is proportional to the MCHC. However, the phase measured by QPI systems is related to both the thickness and the refractive index of the cell (as described by Eq. (1)). Several techniques have been employed to simultaneously measure both n_{RBC} and $h(x, y)$ in order to retrieve MCHC from the former.

One common method is to take images at either two different wavelengths or to use two different immersion media. From the two phase images obtained in each case, one can solve for n_{RBC} and $h(x, y)$ and compute MCHC using the refractive increment α (using Eq. (4)), values of which have been extensively published in literature. MCH can then be computed from MCHC and the measurement of MCV as described in the previous section [20, 22, 34, 57, 58].

Another method has used optical tweezers in combination with QPI to decouple the refractive index and thickness in the phase maps [51]. The optical tweezers can be used to rotate an individual cell and obtain its phase image in two orthogonal orientations $\phi_h(x, y)$ and $\phi_v(x, y)$ (horizontal and vertical). With these two images obtained the refractive index of the cell n_{RBC} can be computed as

$$n_{\text{RBC}} = n_m + \frac{\phi_{v, \max} \lambda}{2\pi d}. \quad (6)$$

Where $\varphi_{v, \max}$ is the maximum value of phase in the vertical orientation, d is the length of the cell along its major axis (assuming elliptical cross-section) and n_m is the refractive index of the solution surrounding the cell. Once n_{RBC} is known, the cell thickness map can be determined from $\varphi_h(x, y)$ using Eq. (5) [51].

As described earlier, tomographic QPI systems that can construct 3D refractive index maps have been developed allowing direct determination of Hb content from the acquired image. As illustrated in Figure 2, cDOT has been employed to study the differences in Hb content between normal individuals (Figure 2b) and individuals suffering from pathologies such as iron deficiency anemia (IDA) (Figure 2c), reticulocytosis (Figure 2d) and hereditary spherocytosis (HS) (Figure 2e) [44].

Tomographic Phase Microscopy (TPM) has also been employed for measuring 3D refractive index maps of RBCs [3, 11]. The TPM optical setup is shown in Figure 3a. In contrast with cDOT, TPM combines phase-shifting interferometry with Computed Tomography (CT), a tomographic technique commonly used in X-ray imaging, to perform 3D reconstruction. The illumination angle on the sample is varied using a Galvanometric Mirror (GM) and for each illumination angle a phase image is obtained from the interferogram formed between the sample and reference fields as described for phase-shifting interferometry in Section 1 of the Supporting Information section [17]. In order to generate the four frames required for phase computation (using Eq. (1.2) in the Supporting Information section), the phase difference between the reference and sample waves is modulated in increments of $\pi/2$ using acousto-optics modulators AOM1 and AOM2 [17]. According to Eq. (1), each of the phase images measured in this way is related to the integral of refractive along the light propagation direction and can hence be thought of as a projection of the refractive index. This is analogous to the projection of absorption typically measured in X-ray CT. Thus, the filtered-back projection algorithm, commonly used in X-ray CT, can be employed for 3D refractive index reconstruction by combining the phase images acquired at each angle [11].

As discussed in Ref. [3], TPM has been used to study the changes in Hb content in RBCs due to infection by plasmodium falciparum, the parasite responsible for malaria. Figure 3b shows the results obtained using TPM for the MCHC (Figure 3b(2)) and MCH (Figure 3b(4)) of plasmodium falciparum infected RBCs (Pf-RBCs) at various stages of the parasite's intra-erythrocytic development. As shown, the results reveal that both MCHC and MCH of infected cells decrease as the disease reaches more advanced stages. Similar conclusions, using QPI of Pf-RBCs, were also drawn by researchers in Ref. [59].

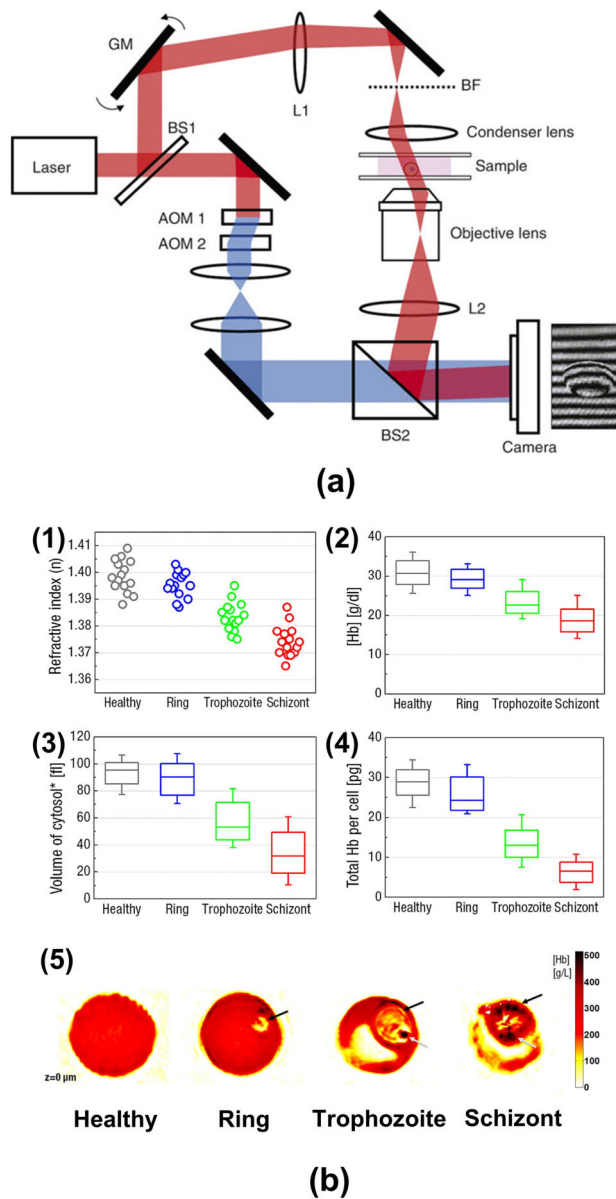


Figure 3 (a) Optical setup for Tomographic Phase Microscopy (TPM). Adapted with permission from Ref. [11] (b) Comparison between healthy RBCs and Pf-RBCs at various stages of parasitization in terms of (1) Average cell refractive index (2) MCHC (3) Cytosolic volume (4) MCH for $N = 15$. The boxes in the box plots represent median and standard deviation while the whiskers represent maximum and minimum values for the group. The Cytosolic volume in (3) was obtained by subtracting the volumes of parasite vacuoles from the total cell volume. (5) Spatial variation of MCHC for cells in each state, extracted from TPM 3D refractive index maps. Adapted with permission from Ref. [3].

Such studies shed light on specific biological mechanisms that can be markers for disease and can be targeted while developing new treatment methods [3].

Other studies have looked at the Hb content of sickle RBCs (Refs. [53, 60]), of RBCs in umbilical cord blood of new-born infants (Ref. [54]) and of RBCs in storage for the purposes of blood transfusions (Ref. [55]) and have compared them with Hb content of RBCs in respective control groups.

3.3.4 RBC dynamics

RBCs endure extreme deformations when they travel through blood vessels and organs by squeezing through capillaries much smaller than their diameter. The mechanical properties of the RBC membrane allow this deformation and maintaining these properties is crucial in order for the cell to successfully transport oxygen [61–63]. The mechanics of the RBC membrane are determined by the phospholipid bilayer and its interaction with the spectrin cytoskeleton [64, 65]. RBC membrane dynamics offer a window into their mechanical properties. Measurement of these dynamics can be used to extract elastic moduli of the membrane based on models developed by scientists over the years [66–68].

As cells go into diseased states their membrane mechanical properties and dynamics change. Thus, probing dynamics can be the basis for classifying cells in various disease states and assessing the health of the patient. Conventional methods for measuring these dynamics include electric field deformation, micropipette aspiration, optical tweezers and magnetic bead excitation. These methods have been limited in their ability to resolve spatial infor-

mation and have the disadvantage of involving contact with the cells.

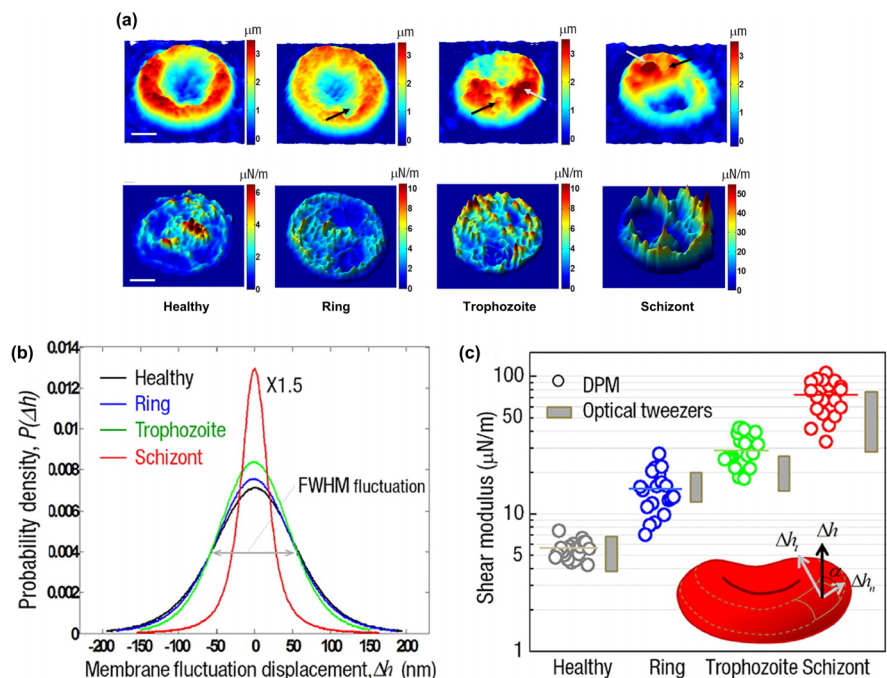
OPI's ability to overcome these limitations has generated interest in its application for studying RBC membrane dynamics. By acquiring a stack of phase images in time and extracting the dynamic height map of the cell $h(x, y, t)$, using Eq. (5), one can compute the membrane fluctuation displacement $\Delta h(x, y, t)$ as

$$\Delta h(x, y, t) = h(x, y, t) - \langle h(x, y, t) \rangle_t, \quad (7)$$

where $\langle \rangle_t$ operation refers to a temporal average. Several important elastic moduli can be extracted from $\Delta h(x, y, t)$: for example the stiffness map $k_e(x, y)$ of the cell is inversely proportional to height map time variance $\langle \Delta h(x, y, t)^2 \rangle_t$.

In Ref. [3], the authors used this analysis to study the mechanical properties of human RBCs parasitized by plasmodium falciparum, a parasite responsible for malaria in humans, at different stages of disease. Representative optical path-length maps of RBCs in each disease stage are shown in the top-row of Figure 4a. Figure 4b shows the histograms of $\Delta h(x, y, t)$ for cells in each of the four different disease stages. The topographic maps used for this computation were extracted from phase images obtained using DPM (described in Section 3.3.2). The $\Delta h(x, y, t)$ histogram narrows as the parasitized RBCs advance in their disease state from Healthy to Schizont stage where extensive remodeling of structure and Hb concentration has taken place. The $\Delta h(x, y, t)$ data were also used to compute the stiffness maps $k_e(x, y)$ and the average in-plane shear

Figure 4 Application of DPM for measuring RBC mechanical properties: Comparison of Pf-RBCs at different stages of parasitization in terms of their (a) $h(x, y)$ maps (top row) and $k_e(x, y)$ maps (bottom row) (b) $\Delta h(x, y, t)$ histograms, scale bar: 1.5 μm . (c) average in-plane shear modulus G value. $k_e(x, y)$ maps were obtained from their inverse proportionality relation with $\langle \Delta h(x, y, t)^2 \rangle_t$ while G was obtained from Δh_t the resolved tangential component of Δh as illustrated in insert of (c) and detailed in Ref. [3]. Adapted with permission from Ref. [3].



modulus G for the cell membranes. Figure 4a (bottom row) and c plot these moduli against progression of disease. According to these results, disease progression in the cells is marked by a dramatic increase in both the stiffness and shear moduli of the cells. These results shed light on how the membrane deformability required in a healthy individual's cells can be altered by a disease like malaria, to the detriment of that individual's health Ref. [3].

Measurement of $\Delta h(x, y, t)$, through QPI, can also be used in other contexts to probe the health of RBCs. When RBCs are subjected to an external stress such as osmotic pressure the cell morphology transitions from the normal Discocyte (DC) state to either Echinocyte (EC) or Spherocyte (SC) morphology, depending on the nature of the stress. These morphological transitions have been shown using QPI to correlate with changes in membrane elastic properties [4]. Figure 5 shows the stiffness maps $k_e(x, y)$ obtained from topographic maps of cells in three different morphological states, acquired using DPM. The data show that an RBC becomes stiffer as its morphology deviates from that under homeostasis, reducing the cell's ability to deform sufficiently for passage through capillaries and, hence, its ability to transport oxygen [4].

The analysis of membrane dynamics has also been used to separate healthy RBCs from diseased sickle RBCs. In Ref. [69], the authors did such an analysis using Wide-field digital Interferometry (WDI). The WDI optical setup shown in Figure 6a. WDI employs a separate path off-axis interferometer, with laser illumination, in a Mach-Zehnder geo-

metry. It generates an interferogram between the sample $U_s(x, y)$ wave and reference wave U_r from which the phase map $\phi(x, y)$ can be extracted using the off-axis phase reconstruction methods described in Section 1 of the Supporting Information section [17]. From the time-resolved phase-maps extracted using WDI, the authors measured $\langle \Delta h(x, y, t) \rangle_t$ to separate healthy RBCs from: (1) morphologically normal or round RBCs obtained from a patient suffering from sickle cell anemia (SCA) and (2) RBCs with a sickle cell morphology, also obtained from a SCA patient.

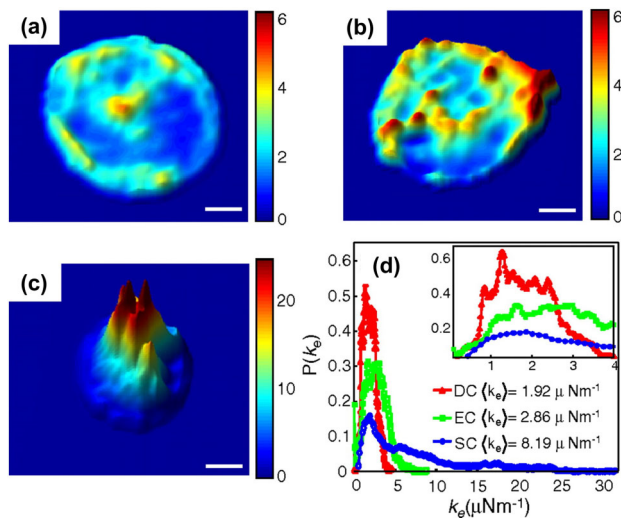
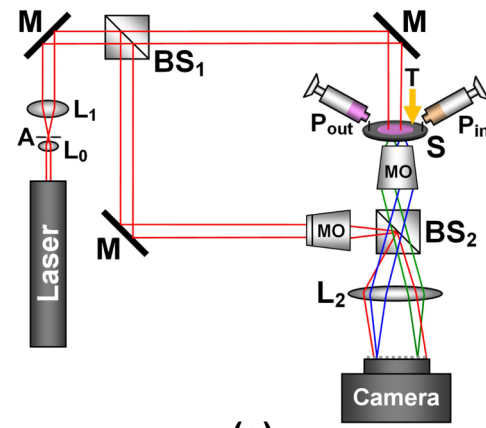
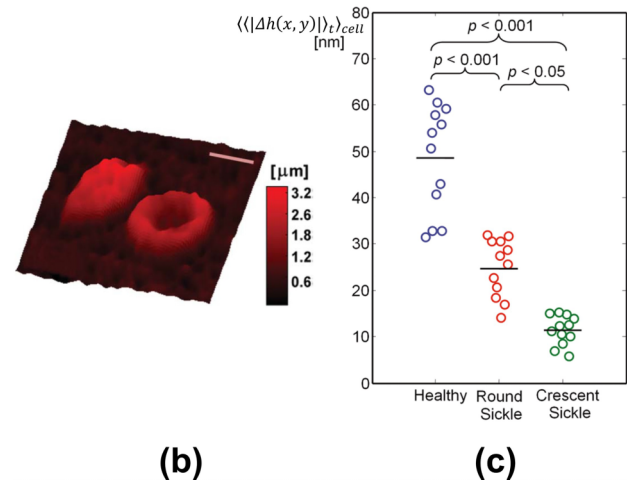


Figure 5 Comparison between spring constant maps $k_e(x, y)$ of (a) Discocyte (DC) (b) Echinocyte (EC) (c) Spherocyte (SC). (d) Histogram of k_e for DC, EC and SC. Color bars are in μNm^{-1} . Legend shows mean k_e for each type of cell and inset shows a zoomed in portion of the histogram plot near the origin. Adapted with permission from Ref. [4].



(a)



(b)

(c)

Figure 6 (a) Optical setup for Wide-field Digital Interferometry (WDI). Adapted with permission from Ref. [70] (b) Optical-path length map of a morphologically normal (right) and sickle shaped (left) cells, obtained using WDI. (c) $\langle \langle \Delta h(x, y) \rangle \rangle_{t, \text{cell}}$ for three types of cells at various stages of disease. Each data point refers to a single cell and the horizontal lines represent average value for the group. Statistical significance of the difference between groups was determined using the two-side Wilcoxon rank sum test. The healthy cells were obtained from one individual while the round sickle and crescent sickle cells were obtained from two individuals. Adapted with permission from Ref. [69].

The results are summarized in Figure 6b and c. As shown the $\langle\langle\Delta h(x, y)^2\rangle\rangle_{\text{cell}}$ value for these three types of RBCs (where $\langle\rangle_{\text{cell}}$ refers to cell average) was significantly different, indicating that the onset of SCA is marked by an increase in stiffness of the cell membrane. Other works have also measured membrane fluctuations to investigate sickle cell disease progression and its effect on cell membrane mechanical properties as demonstrated in Refs. [60] and [53].

Another area of interest has been the diagnosis of RBC health in stored blood and quantifying the effects of storage lesion. Determining whether RBCs in stored blood are healthy and viable is crucial for patients requiring transfusions. In Ref. [71], the authors describe a diagnostic method for assessing stored RBC health using a phase-shifting QPI technique called Spatial Light Interference Microscopy (SLIM).

SLIM is a common-path, white-light based system built as an add-on module to a commercial phase contrast microscope, as illustrated in Figure 7a [72]. As shown, the image plane at the output of the microscope is relayed onto the camera plane by a 4-f system formed by lenses L_1 and L_2 . A Liquid Crystal Phase Modulator (LCPM) is placed at the Fourier plane of lens L_1 . The LCPM introduces four different phase shifts (in increments of $\pi/2$) between the unscattered and scattered portions of light leading to four distinct interferograms. From these interferograms the phase image can be extracted using the reconstruction method for phase-shifting interferometry described in Section 1 of Supporting Information section and detailed in Ref. [72].

The authors analyzed the stored RBC membrane displacement maps, acquired using SLIM, to shed light on how the elasticity of these cells deteriorates with storage time. Their results are summarized in Figure 7b–d. The variance $\langle\langle\Delta h(x, y, t)^2\rangle\rangle_{\text{cell}}$ for the measured RBCs continues to decrease as the storage time increases from 0–6 weeks. $\langle\langle\Delta h(x, y, t)^2\rangle\rangle_{\text{cell}}$ is inversely proportional to mean cell stiffness $\langle k_e \rangle_{\text{cell}}$ which means that, over time, stored RBCs become stiffer. In blood storage banks this analysis can thus potentially be used to conveniently assess whether RBCs are viable for transfusions. QPI works particularly well for this application because it is able to diagnose the viability of stored RBCs in a label-free, non-invasive and spatially resolved manner [71]. Other works have also used a similar analysis to quantify the effect of storage lesion on RBCs and their viability for transfusions [55, 56].

3.3.5 RBC light scattering

Elastic light scattering (ELS) measurements can provide information about the structure and dynamics of biological specimen [73, 74]. Specifically, if one

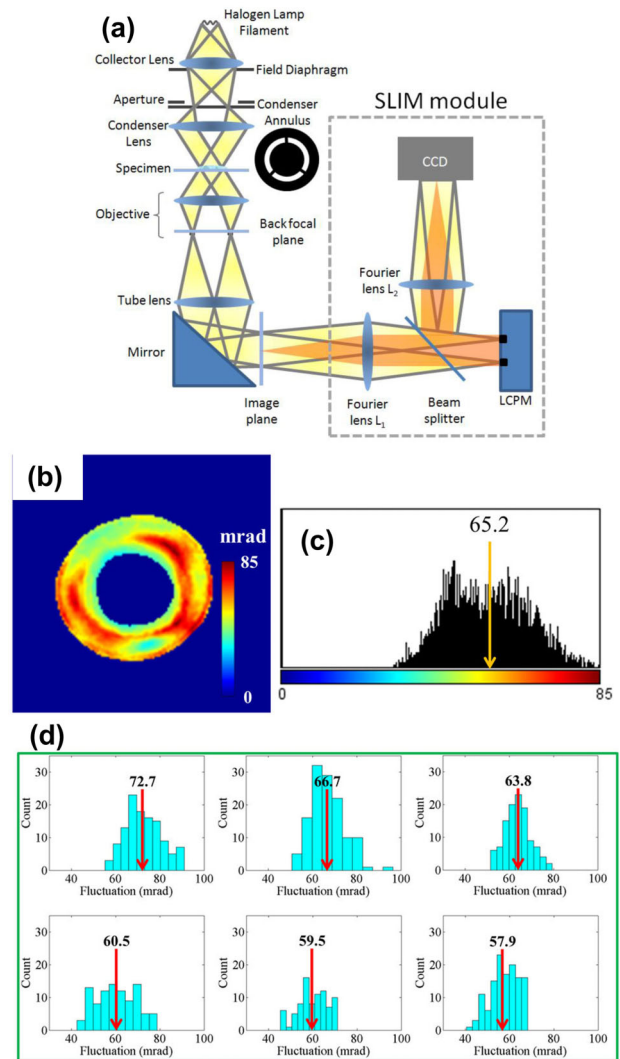


Figure 7 (a) Optical setup of Spatial Light Interference Microscopy (SLIM). (b–d) Variation of cell membrane stiffness with storage time (b) Temporal standard deviation of phase σ_t for a single RBC which is proportional $\langle\Delta h(x, y, t)^2\rangle$, which in turn is proportional to stiffness $k_e(x, y)$. (c) Histogram of image in (b) with average value shown (d) Changes in histogram with storage time from 1–6 weeks. Decrease in average value is indicative of increase in average cell stiffness. Adapted with permission from Ref. [71].

can map the angular distribution of the scattered field, the structure of the object can be characterized from this distribution. The angular distribution of the far-field scattered field $U(\mathbf{k})$ is related to the complex object field $U(\mathbf{r})$ through its Fourier transform as

$$U(\mathbf{k}) = \int U(\mathbf{r}) e^{-i\mathbf{r} \cdot \mathbf{k}} d^2\mathbf{r}, \quad (8)$$

where \mathbf{k} is the spatial wave vector that can be related to the scattering angle [9, 75]. Since QPI instru-

ments allow the measurement of $U(\mathbf{r})$, obtaining the scattered field boils down to numerically taking the Fourier transform of $U(\mathbf{r})$. Thus, QPI can be used to make angular-scattering measurements without the need for complex rotating detectors or goniometers. For this reason, this method has been referred to in the literature as Fourier Transform Light Scattering (FTLS) [9, 76–78].

This methodology has been employed to study the characteristics of RBCs in various disease states. Figure 8 shows the results of a study done on human sickle RBCs. The authors used DPM to obtain time stacks of the complex image field $U(\mathbf{r}, t)$ for type II, III and IV sickle RBCs as well as for a healthy control. The angular distribution of the far-field scattering field was then calculated for each frame using Eq. (8). The temporal autocorrelation of the scattering field at each angle was then calculated and fit with a damped cosine function. The peak frequency ω_0 and line width Γ for the damped cosine was determined for each scattering angle. These maps were then used to calculate ω_0 and Γ along the long and short axes of the sickle cell as detailed in Ref. [79]. As shown in Figure 8 these two metrics were different for cells at different stages of disease, reflecting the biochemical and biomechanical modifications caused by disease progression. Such scattering studies using QPI where information along specific axes is obtainable without the need for complicated detection geometries have the potential to rapidly elucidate biological events that are characteristic of the disease state.

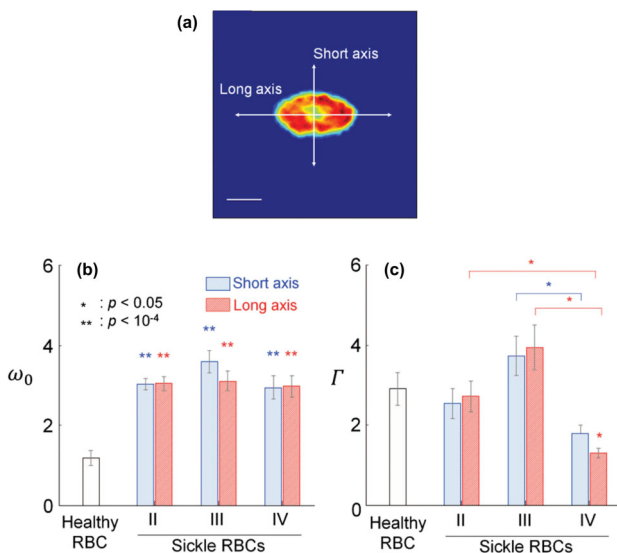


Figure 8 (a) Typical phase image of a sickle RBC obtained using DPM. (b) Peak frequency ω_0 and (c) line width Γ , that parameterize the temporal autocorrelation of the scattering field, measured along the short and long axis of sickle RBC. Error bars indicate standard error. Adapted with permission from Ref. [79].

3.4 QPI for White Blood Cell (WBC) screening

As mentioned earlier, the bulk of the work done using QPI techniques for blood analysis has involved studies of RBCs. This is due to the fact that RBCs have a simple homogenous structure which simplifies analysis and samples of RBCs are easier to prepare due to their relative abundance in blood compared to WBCs. However, in the clinical workflow differential WBC counts and analysis are critical to diagnosis. While a number of recent biological studies have involved QPI imaging of WBCs, assessment a patient's hematological health vis a vis QPI of WBCs remains a relatively unexplored area [80–83].

Figure 9 summarizes a study performed on mouse WBCs using QPI. In this study, Mach-Zehnder Interferometric Microscopy was combined with Computed Tomography (CT) to generate 3D refractive index maps for mouse lymphocytes and macrophages. As shown in Figure 9a, the optical setup for this QPI technique features a rotating 2D Galvanometric Mirror (GM) which scans the angle of illumination on the sample. For each illumination angle, a separate path laser-based Mach-Zehnder interferometer is used to generate an off-axis interferogram between the sample and reference waves from which the phase can be extracted using standard off-axis reconstruction methods (see Section 1 in Supporting Information section) [17]. An Optical Diffraction Tomography (ODT) algorithm is then used to reconstruct the 3D refractive index tomogram for the cells by combining the data acquired at each angle, as described in Ref. [84]. In this study, the authors extracted geometric parameters and cell dry mass from the measured WBC refractive index tomograms using methods discussed earlier in the context of RBCs. As shown in Figure 9b, these parameters are markedly different between lymphocytes and macrophages, providing a potential basis for label-free classification of these cells with microscopic resolution.

Figure 10 illustrates another example of a QPI study done on WBCs. In this study, the authors investigated the effects of bacterial infection on mouse macrophages by imaging them using Digital Holographic Microscopy (DHM). DHM is a laser-based, off-axis separate path QPI method that typically employs the Mach-Zehnder geometry for generating an interferogram between the sample and reference waves, similar to Mach-Zehnder Interferometric Microscopy and WDI discussed earlier in the text. The optical setup used in this study is illustrated in Figure 10a. Phase reconstruction from the acquired interferogram follows the standard procedures for off-axis interferometry discussed in Section 1 of Supporting Information section [17, 86–88].

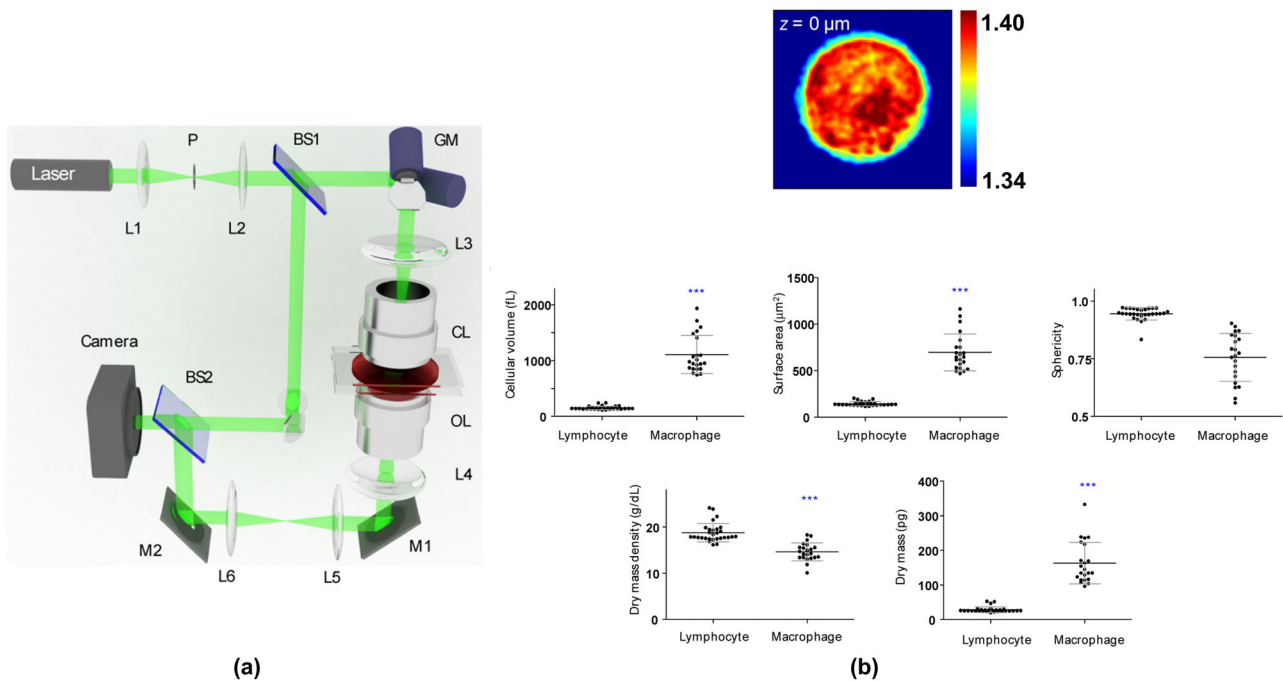


Figure 9 (a) Optical setup of Mach-Zehnder Interferometric Phase Microscopy. (b) Comparison of 3D morphological parameters and cell dry mass for lymphocytes and macrophages extracted from 3D refractive index maps generated by tomographic QPI. Color bar represents refractive index. Each data point represents measurement for one cell, horizontal lines represent averages and vertical lines represent standard deviation ($N = 29$ for lymphocytes and $N = 22$ for macrophages). *** indicates a p -value < 0.001 when comparing lymphocytes and macrophages using Student's t -test. Adapted with permission from Ref. [84].

As shown in Figure 10b, the authors compared the average cell refractive indexes of infected and normal mouse macrophages. The cell refractive index maps were extracted from the raw phase maps

by assuming a spherical shape for the macrophages, allowing estimation of the cell thickness from the radius of its circular cross-section. As the data show, the infected macrophages had a significantly lower

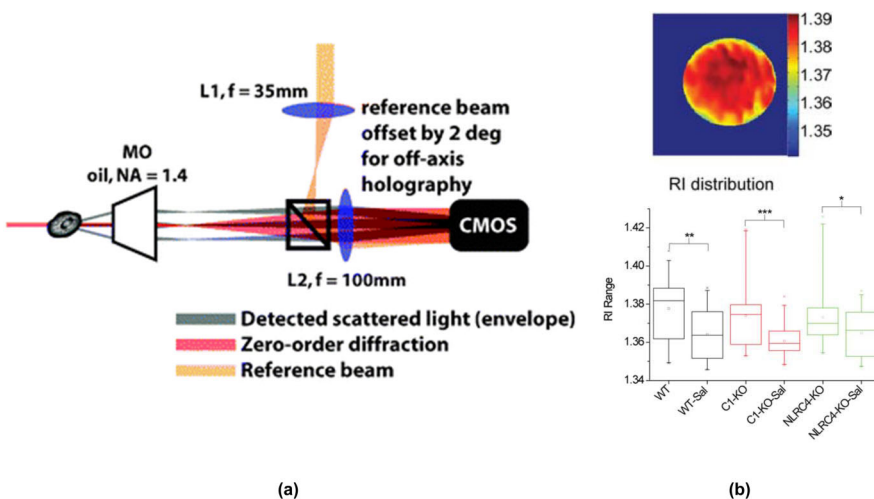


Figure 10 (a) Optical setup of the Digital Holographic Microscopy (DHM) setup used in this study. Adapted with permission from Ref. [82]. (b) Effect of *Salmonella enterica* serovar Typhimurium (Sal) infection on the refractive index of a mouse macrophage, as measured by DHM (Color bar represents refractive index). In each case the infected WBC shows a lower refractive index on average compared with the control. Knocking out genes that may have been responsible for this refractive index decrease did not change the results. *, **, *** represent p -values < 0.05 , 0.01 and 0.001 respectively obtained from standard one-way parametric ANOVA test. Adapted with permission from Ref. [85].

refractive index than corresponding control (uninfected) macrophages, making the refractive index a marker for infection [85].

4. Cancer diagnosis using QPI

4.1 Introduction

According to the World Health Organization (WHO), cancer is one of the leading causes of illness and mortality in the world with 8.2 million deaths reported worldwide in 2012 [89]. This grim assessment has led to extensive research over the years on better diagnosis and prognosis methods. The National Institute of Health (NIH) estimated that it awarded research grants totaling around \$ 5.4 billion for cancer research in 2014 [90].

Pathologists diagnose cancer through microscopic observation of suspicious tissue extracted from patients following a biopsy procedure or surgery. The extracted tissue is first subjected to dehydration and fixation in formalin, followed by embedding in paraffin. The resulting tissue is referred to as Formalin Fixed and Paraffin Embedded (FFPE). Thin tissue slices of 4–5 microns are then cut using a microtome and placed on a glass slide. These slices are then stained after de-paraffinization and re-hydration. Staining is required because optically thin slices of tissue do not significantly scatter or absorb light, making them transparent. Tissue biopsy sections are traditionally stained with Hematoxylin and Eosin (H&E). Hematoxylin stains nucleus in a deep blue-purple by a reaction that is not completely understood, whereas eosin non-specifically stains proteins pink and makes the cytoplasm and extra-cellular matrix visible [91]. H&E double stain was first introduced in 1876 by Wissowzky and, more than a century later, continues to be the most frequently used staining method in diagnostic pathology [92]. After staining, the pathologist examines the tissue under a microscope in order to make a diagnosis. When the pathologist suspects the presence of cancer on the H&E stained biopsy, a consecutive biopsy section is stained with specialized stains and immunohistochemical markers (IHC) to make a final diagnosis.

Formalin fixation has been reported to damage or mask antigen sites to which IHC antibodies bind [93]. Antigen preservation in frozen tissue has been reported to be better than in FFPE tissue and alcohol fixation represents an intermediate option for antigen preservation [94]. However, FFPE is the most common histological method used internationally [95, 96]. Other problems in immunohistochemistry include the definition of a positive stain, which is

subject to variation based on the tissue compartment where a positive stain was seen (center of the tumor versus the periphery), pattern of the staining (cellular compartment: cytoplasm versus the nucleus) and staining intensity that can be considered positive [97]. All of these sources of variation contribute to inter-observer variability in interpretation of IHC results. Many computer-assisted IHC interpretation methods are in development today, in an attempt to make interpretation quantitative and thus standardized [98]. However, these methods are still subject to variations in interpretation stemming from variations in the illumination source, sensor of the camera, intensity of the stain and signal multiplexing [98].

A common theme that emerges from studying innovations in pathology is that the developments have focused on extrinsic tissue markers and pace of clinical adoption is slow. The slow pace could be due to the applicability of each immunohistochemistry marker for a limited number of diseases, thus generating a large number of tests for specific clinical endpoints in each disease. Additionally, some IHC techniques require tissue fixation to be performed in a manner that is different from the standard pathology processing standards thus proving to be cumbersome.

Structural information in tissue holds enormous diagnostic potential, as evidenced by the permanence of non-specific stains, such as H&E, in pathology practice. Cells and tissue also have intrinsic contrast in the form of refractive index differences between various structures. By measuring phase, which is related to the refractive index of tissue, Quantitative Phase Imaging (QPI) reports on nanoscale changes in tissue architecture, while also providing structural information. It uses intrinsic tissue contrast, thus eliminating the need for specialized stains and is insensitive to changes in illumination and camera. In this way, a QPI based method can address the limitations of IHC and H&E based investigations by eliminating inter-observer variability. Additionally, the same imaging modality can be used to report on multiple tissue archetypes, thus reducing the learning curve. As reviewed below, these merits have motivated studies in both diagnosis and prognosis of various types of cancers using QPI.

The QPI studies of cancer discussed below can be broadly separated into two groups: studies involving fixed tissue sections and studies involving single live cells. QPI studies on tissue sections are important in that they quantify differences in tissue level organization in diseased and healthy tissue through measurement of scattering properties and refractive index distribution (Sections 4.2–4.3 and Sections 4.6–4.8). These studies are also significant in quantifying the effect of the tumor microenvironment on disease

progression and explaining the complex interplay between epithelial and connective tissue that marks the progression of several different cancers [99–101]. Studies involving single live cells on the other hand are significant in that changes that occur in cells during malignant transformation can be quantified by investigation of morphology, membrane dynamics as well as cell refractive index (Section 4.4–4.5 and Section 4.9). Furthermore, biochemical interactions of the cell with signaling molecules (such as growth factors), effects of drugs on diseased cells and genomic and proteomic changes in cells (for example changes in gene expression) can also be studied in live single cell cultures [102–105]. Thus, both types of studies can provide complementary information on cell and tissue biology and how it relates to disease.

4.2 Scattering phase theorem

Hallmarks of malignancy include an increase in the number of cells, changes in the organization of stroma and epithelial glands and changes in cellular morphology such as prominent nucleoli. These features lead to changes in the scattering properties of the tissue. The scattering properties of tissue are generally captured by two parameters: l_s the mean distance travelled by light for a single scattering event and g which is the average cosine of the scattering angle θ over a tissue thickness equal to l_s , (also called anisotropy factor). Under the Born approximation for weakly scattering media and tissue thickness L much smaller than l_s , these parameters are

related to ϕ , the phase measured by QPI instruments, as

$$l_s = \frac{L}{\langle \Delta\phi^2(\mathbf{r}) \rangle_r}, \quad (9)$$

$$g = 1 - \frac{1}{2k_0^2} \frac{\langle |\nabla[\phi(\mathbf{r})]|^2 \rangle_r}{\langle \Delta\phi^2(\mathbf{r}) \rangle_r^2}, \quad (10)$$

where $\langle \Delta\phi^2(\mathbf{r}) \rangle_r$ represents the spatial variance of the phase and $\langle |\nabla[\phi(\mathbf{r})]|^2 \rangle_r$ is the spatial average of the magnitude squared of the gradient of the phase [106]. Since in standard tissue processing, biopsy sections are cut into slices that are much thinner than the typical scattering length l_s in tissue, both l_s and g can be extracted by imaging standard unstained FFPE histology slides [106].

These two parameters are numerically computed over appropriate kernel sizes in a phase image to generate their maps. The variation of these maps between malignant and benign tumors has been shown to be a promising basis for diagnosis. Figure 11 shows the results obtained from such an analysis of phase maps of prostate cancer tissue biopsies imaged using Spatial Light Interference Microscopy (SLIM) [107]. Two parallel sections of each tissue biopsy were obtained and one of them was stained with H&E for bright field imaging leaving the other one unstained for SLIM imaging (Figure 11a and e). By looking at the H&E image, a board certified pathologist marked both benign and malignant areas on the tissue section (in green and red respectively) [107].

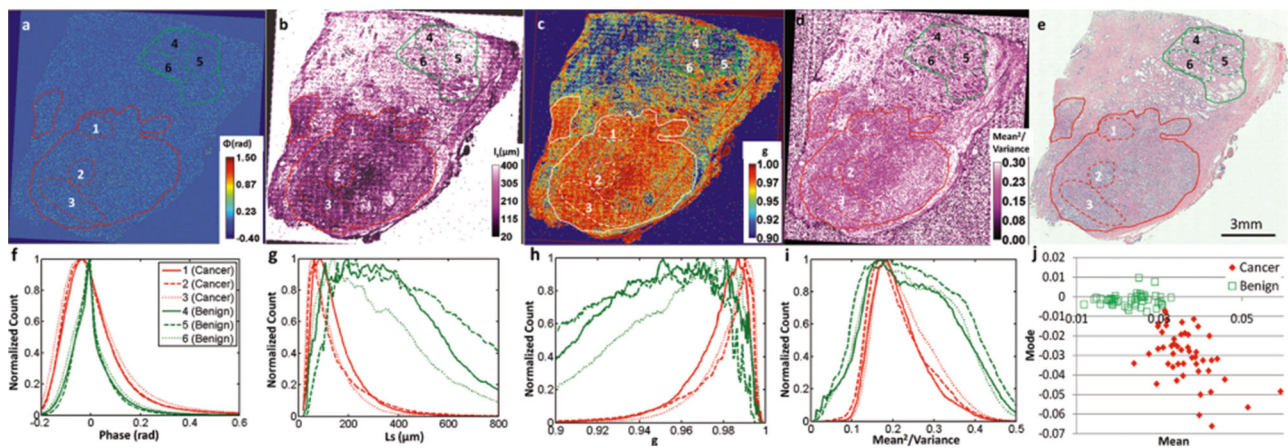


Figure 11 Maps of (a) phase, (b) l_s , (c) g and (d) $\frac{\text{mean}^2}{\text{variance}}$ of phase for a prostate cancer tissue biopsy section. (e) H&E stained tissue image of a parallel section of tissue with benign and malignant tumor areas marked by a pathologist. The same areas are also shown on the other maps. (f–i) Histograms of areas marked in (a–e) respectively. (j) Mode vs. Mean of phase plotted for 49 cancerous and 51 benign areas from 11 different tissue sections from 9 different patients. Adapted with permission from Ref. [107].

As shown in Figure 11b and c, the l_s and g maps computed over benign regions (labelled 4,5,6) are markedly different in terms of pixel values from those computed over malignant regions (labelled 1,2,3). This is also evidenced by the histograms of the two parameters computed over these regions as shown in Figure 11g and h. Similar analyses, using l_s and g maps extracted from phase images, have also been carried out in other publications with the aim of diagnosing cancers and segmenting different tissue regions [108].

4.3 Refractive index as a marker for disease

For thin tissue sections the phase obtained by QPI modalities can be considered directly proportional to the refractive index of tissue. This is because for thin sections the changes in tissue thickness are very small at spatial scales corresponding to the size of a cell, which is the scale over which parameters are often computed. FFPE biopsy sections are generally around 4–5 μm thick and satisfy this requirement at

the spatial scale of one cell, in spite of cutting errors that might be present. For such sections the phase image is essentially a map of refractive index and informs on the composition and organization of tissue. This was evidenced in the study described in Ref. [109] where the authors imaged mouse liver, spleen and brain tissue using a QPI technique called Hilbert Phase Microscopy (HPM). The HPM optical setup is shown in Figure 12a. As shown, HPM uses a laser-based separate path interferometer in the Mach-Zehnder geometry to generate an off-axis interferogram between the sample and reference waves from which phase reconstruction can be carried out as described in Supporting Information Section 1 [17].

The authors in Ref. [109] used HPM to show that the three different types of mouse organ tissue had significantly different refractive indexes as well as significantly different decay lengths of the spatial power spectra of their respective images. They further went on to show that, using tissue refractive index as a marker, lysosomal storage disease (LSD) in mouse liver tissue may be diagnosed. As shown in Figure 12b–e, the reported standard deviation of refractive index for diseased tissue was significantly

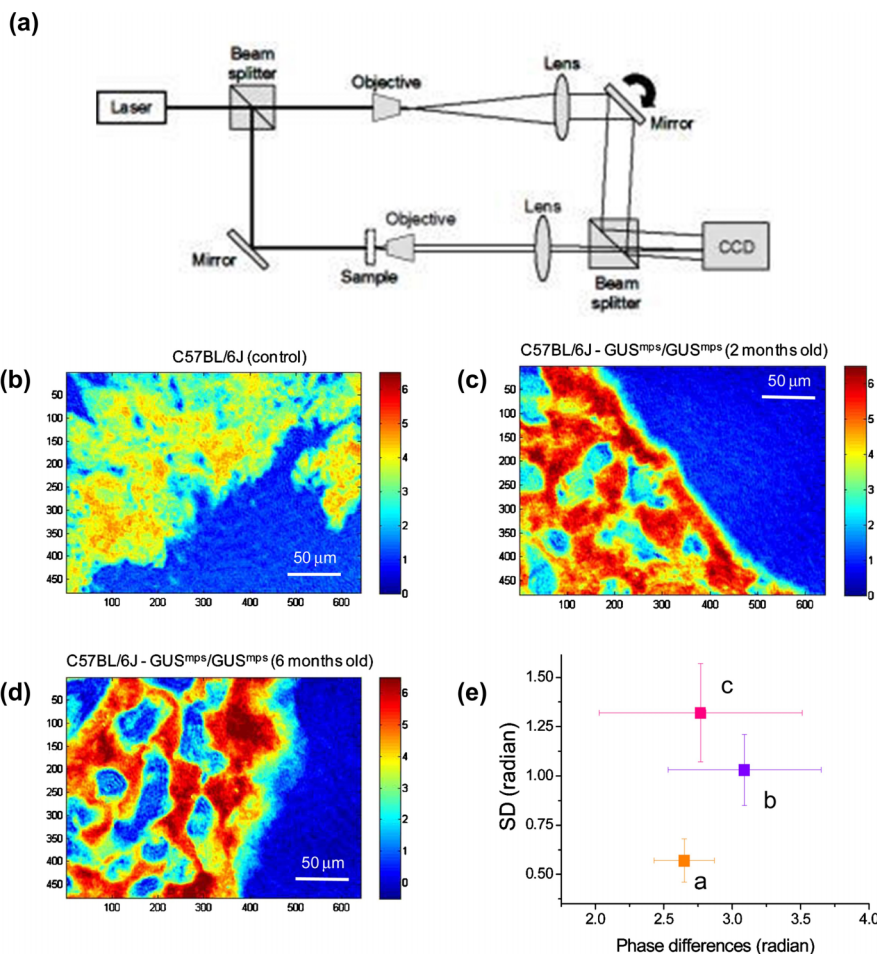


Figure 12 (a) Optical setup of Hilbert Phase Microscopy (HPM). Adapted with permission from Ref. [110] (b–e) Comparison between phase maps of (b) healthy mouse liver tissue (c) tissue with lysosomal storage disease after 2 months (d) tissue with lysosomal storage disease after 6 months. (e) The standard deviation of the phase maps of these tissues are shown to be significantly different. Adapted with permission from Ref. [109].

different from that of the healthy control – offering a means of diagnosing LSD in mouse liver tissue with potential implications for similar analyses on human tissue [109].

These results also motivated investigations into how refractive index maps vary between benign and cancerous tissue. In the study on prostate cancer diagnosis summarized in Figure 11 (and introduced in the previous section), the statistics of ϕ and $\frac{\text{mean}^2}{\text{variance}}$ of ϕ were significantly different between the benign (green) and malignant (red) areas as evidenced by their respective histograms (Figure 11f–i). There was maximum separation between the data clusters corresponding to benign and malignant regions when plotted in mean versus mode space (Figure 11j). These results showed that refractive index maps inform on tissue homogeneity and organization and can, hence, be used as a quantitative label free marker for diagnosis in patients with prostate cancer [107].

A series of other publications have looked specifically at the refractive indices of epithelial cell nuclei as markers for malignancy and cancer progression in different types of tissue. These works have employed a white-light common-path QPI method called Spatial-domain Low-coherence Quantitative

Phase Microscopy (SL-QPM) to measure the epithelial cell refractive index maps. We will briefly describe the operating principle SL-QPM before discussing the results of these publications.

Figure 13a illustrates the optical setup of SL-QPM, which employs reflection mode microscopy of tissue samples. As shown, the system uses a broadband source (Xenon arc lamp) which is collimated using a 4f system (lenses L1 and L2). A beam-splitter (BS) is used to separate the incident light from the light reflected off the sample (which is collected by the microscope objective (OB1)). This reflected light is then collected by a tube lens (TL) and imaged onto both a conventional camera for back-scattering measurements and a spectrograph coupled to a CCD camera for phase imaging. The spectrograph/CCD combination is mounted onto a translation stage that is moved along the x -axis. At each step of the scan, the CCD records a matrix whose x -axis represents wavelengths and whose y -axis represents the y -coordinate of the sample image. As a result, the final image comprises of a 3-D intensity cube $I(x, y, \beta)$ where β represents the wave number. Since the intensity image is formed by interference between the sample $U_s(x, y, \beta)$ and reference U_r fields, it is given by Eq. (11) below. The reference field is

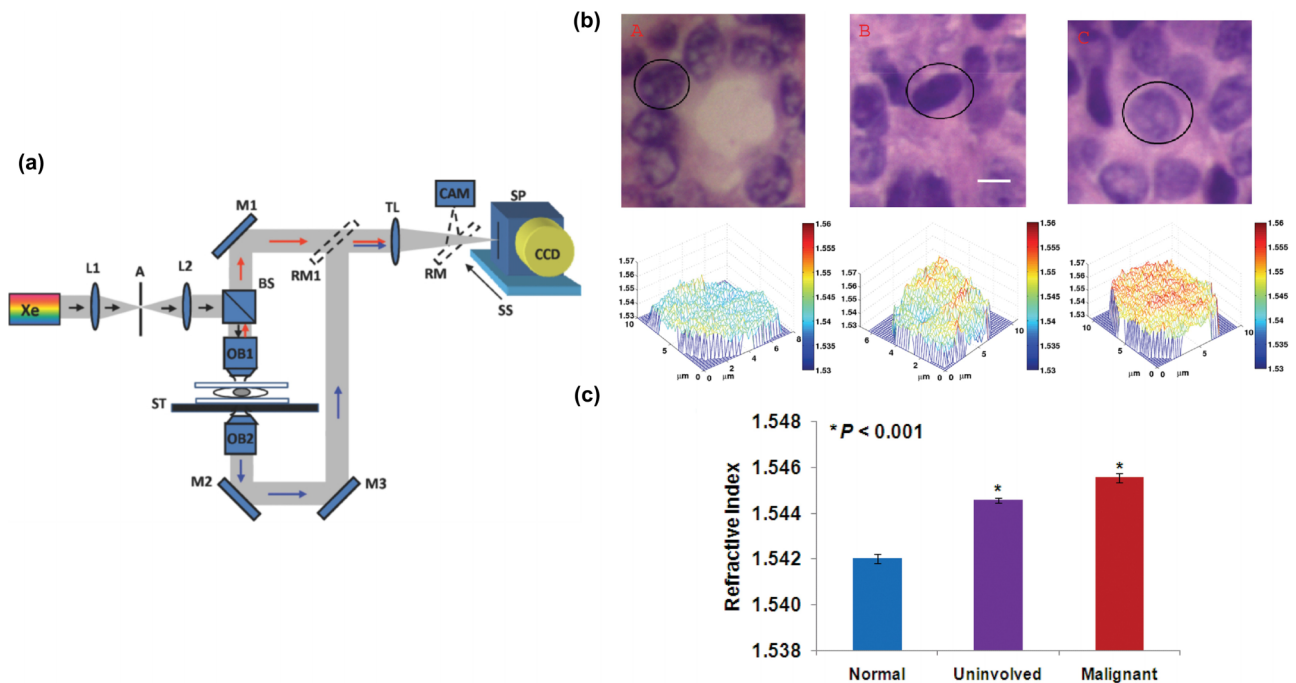


Figure 13 (a) Optical setup of Spatial-domain Low-coherence Quantitative Phase Microscopy (SL-QPM). Adapted with permission from Ref. [111]. (b) Stained histology images and refractive index maps of cell nuclei from A. Normal, B. Uninvolved and C. Malignant breast epithelial cells. Scale bar: 5 μm . The refractive index map is shown for the circled cell nucleus in each case. (c) Average cell refractive index is higher in the uninvolved and malignant cases compared to normal case. A two-sided Student's t -test was performed to test for significance of separation. Samples in each group were obtained from 5 patients and the data shown is from 30 cell nuclei in each group. Adapted with permission from Ref. [112]

generated in this case by the light reflecting off the glass substrate [111].

$$I(x, y, \beta) = |U_r(\beta)|^2 + |U_s(x, y, \beta)|^2 + 2|U_s(x, y, \beta)| |U_r(\beta)| \cos [\phi(x, y, \beta)]. \quad (11)$$

The phase map $\phi(x, y)$ can be extracted from the above intensity image as follows. After some denoising steps [111, 112], the axial spatial cross-correlation function $F(x, y, z)$ is obtained for each pixel by computing the Fourier transform of $I(x, y, \beta)$ along the β dimension [113]. In order to compute the phase map, for each pixel, a single value of $F(x, y, z)$ is chosen at the prominent peak corresponding to the optical path length of interest [111, 112]. From the resulting two-dimensional data $F(x, y)$, the phase image can be computed as

$$\phi(x, y)|_{(z, \nu)} = \tan^{-1} \left\{ \frac{\text{Im} [F(x, y)|_{(z, \beta)}]}{\text{Re} [F(x, y)|_{(z, \beta)}]} \right\}. \quad (12)$$

As mentioned, SL-QPM has been used in a number of clinical studies that have involved measurement of the refractive index maps of epithelial cell nuclei. In Ref. [112], SL-QPM was used to compare the refractive index maps of nuclei of breast epithelial cells from normal patients, normal breast epithelial cells from cancer patients (uninvolved) and malignant breast epithelial cells from cancer patients. The refractive index maps were extracted from phase images by assuming constant tissue thickness. As summarized in Figure 13b and c, the authors of this study showed that as malignant transformation occurs in breast epithelial cells, their refractive index increases. One of the key advantages of this technique is that FFPE and H&E stained tissue slides were used, which means that this technique has the potential to be directly incorporated into the standard diagnostic pipeline with minimal changes. An interesting area of study is to quantify the effects of the stain on the phase values measured.

In Ref. [114], the authors used SL-QPM to generate depth-resolved optical path difference (drOPD)

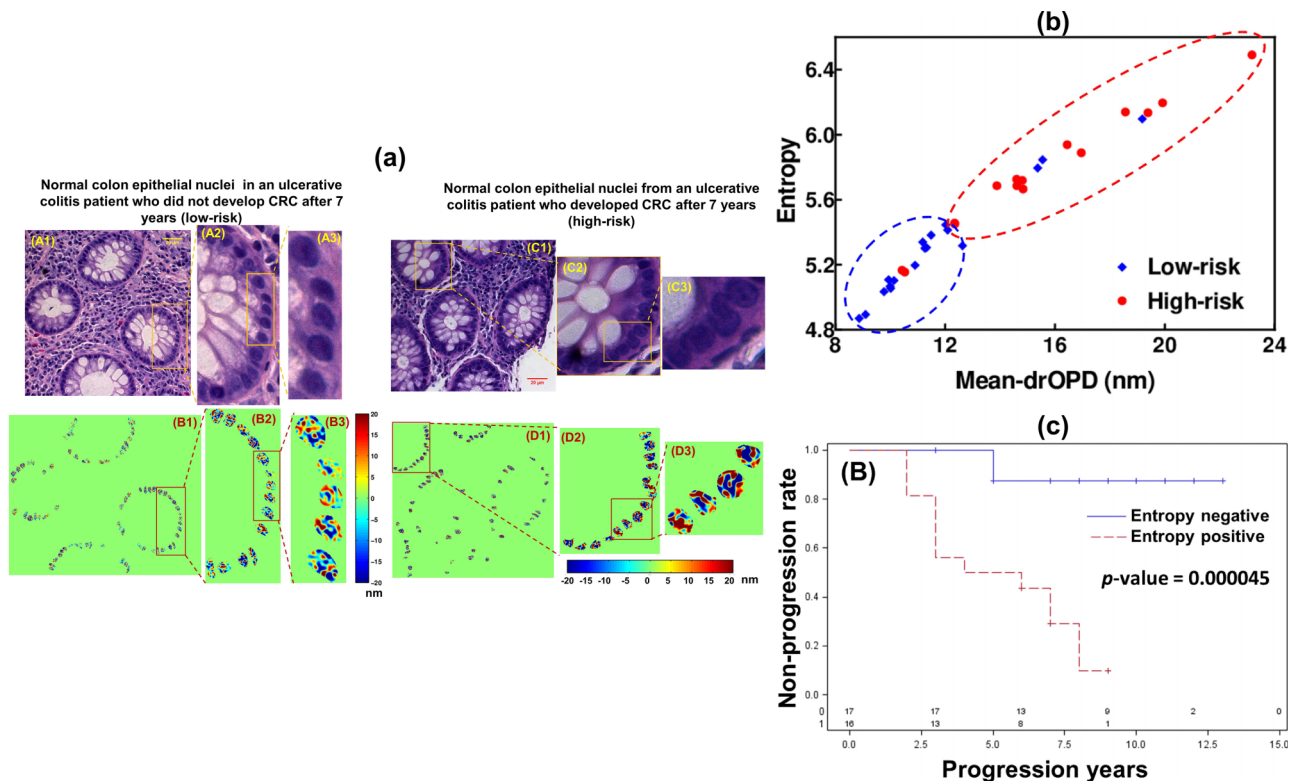


Figure 14 (a) H&E stained tissue bright field images (left) and drOPD maps (right) of colon tissue biopsies from patients suffering from ulcerative colitis, diagnosed as normal by a pathologist. The patients were retrospectively grouped into low-risk and high-risk categories as shown. (b) The two risk categories are separated in the Entropy vs. Mean-drOPD (nm) scatter plot, showing the prognostic potential of drOPD derived parameters. Each data point in the scatter plot refers to a single patient, obtained after averaging over 300 to 600 nuclei per patient. (c) Kaplan-Meier curves using entropy as an estimator. Entropy positive data points are defined as those having an entropy of greater than 5.45. The difference between the Entropy positive and Entropy negative data sets was statistically significantly ($P = 0.000045$ as determined by the log-rank test). Figures courtesy Prof. Yang Liu, University of Pittsburgh [114].

maps of epithelial cell nuclei in colon tissue, diagnosed as normal by a pathologist, to determine the risk for future malignancy. The biopsies, obtained after a surveillance colonoscopy procedure from patients suffering from ulcerative colitis (UC), were retrospectively analyzed to assess the ability of drOPD maps to separate patients that would go on to develop high-grade dysplasia (HGD) or colorectal carcinoma (CRC) (high risk) from those that would not (low risk). The drOPD metric, measured in this analysis, quantifies the nanoscale nuclear architecture through a depth resolved measurement of the refractive index. Figure 14 illustrates the results of this study. As illustrated in Figure 14b, parameters extracted from the drOPD maps (mean-drOPD and Entropy as defined in Ref. [114]) are able to separate the two risk categories. This analysis has the potential to quantitatively predict the risk of occurrence of HGD or CRC in patients so timely treatment measures can be taken. As illustrated in Figure 14c, the entropy parameter (extracted from drOPD maps) was statistically significant in terms of predicting colorectal disease progression when analyzed using Kaplan-Meier (KM) curves.

The refractive index of cell nuclei, measured by SL-QPM, has also been employed as a marker in studies on colorectal cancer [111], “field effect” in breast cancer [115], malignancy in bile duct biopsies [116, 117] and pancreatic cancer [118].

4.4 Cancer diagnosis using cell dynamics

As was discussed in Section 3.3.4, the dynamics of the cell membrane, which are measurable with nanoscale sensitivity using QPI, can inform on its mechanical properties. Since cancer progression is marked by phenotypical changes in a cell, these changes may lead to changes in the cell membrane’s mechanical properties that can be measured using QPI. As published in literature, a QPI method called Wide-field Interferometric Phase Microscopy (IPM) has been used to investigate epithelial cell membrane dynamics [103].

IPM (illustrated in Figure 15) uses a Michelson interferometer to generate an off-axis interferogram between the sample and reference waves. The IPM system has two different versions: the simplified transmission interferometer (Figure 15a) and the Off-axis τ interferometer (Figure 15b), both built as ad-on modules to a commercial bright field microscope [103]. In the simplified transmission interferometer, the image plane at the output port of the microscope is relayed on to the camera plane using a 4f lens system (comprising lenses L1 and L2). A beam splitter is used to split the incoming light into two identical beams that reflect off mirrors M1 and

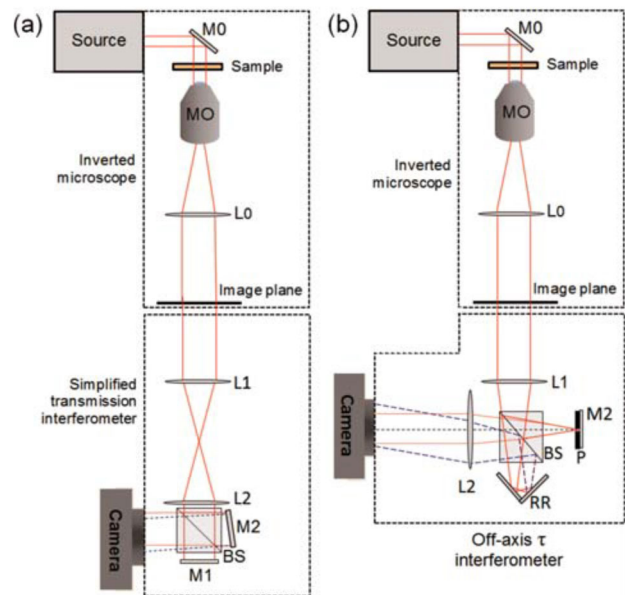


Figure 15 Two different geometries of Wide-field interferometric phase microscopy (IPM): (a) the simplified transmission interferometer. (b) The off-axis τ interferometer. Adapted with permission from Ref. [103].

M2 to generate the image and reference fields, respectively, at the camera plane. The reference field in this interferometer is a spatially shifted version of the image field, generated by rotating mirror M2. Spatial shifting allows one to generate a reference field because by design a portion of the sample has no structure and by adjusting M2, this background can be co-registered with the structural information in the image field to generate an off-axis interferogram. The off-axis τ interferometer, while following the same Michelson configuration, differs from the simplified transmission interferometer in the way the reference field is generated. As shown in Figure 15b, in this system a pinhole is placed in front of mirror M2 to spatially low pass filter the image field in order to generate a reference plane wave. This plane wave then interferes with the image field emerging after reflection from mirror M1 to generate an off-axis interferogram at the camera plane.

In either of the two cases, from the interferogram at the camera plane the phase reconstruction can be performed using the off-axis reconstruction methods described in Section 1 of Supporting Information section [17].

In Ref. [103] IPM was used to compare the dynamics of normal and cancerous rat intestinal epithelial cells as well as those of primary human colorectal carcinoma cells and their metastatic counterparts. The fluctuation maps were calculated by acquiring a time-stack of quantitative phase images and computing their standard deviation (STD) in time (as also discussed in Section 3.3.4). The results are summarized in

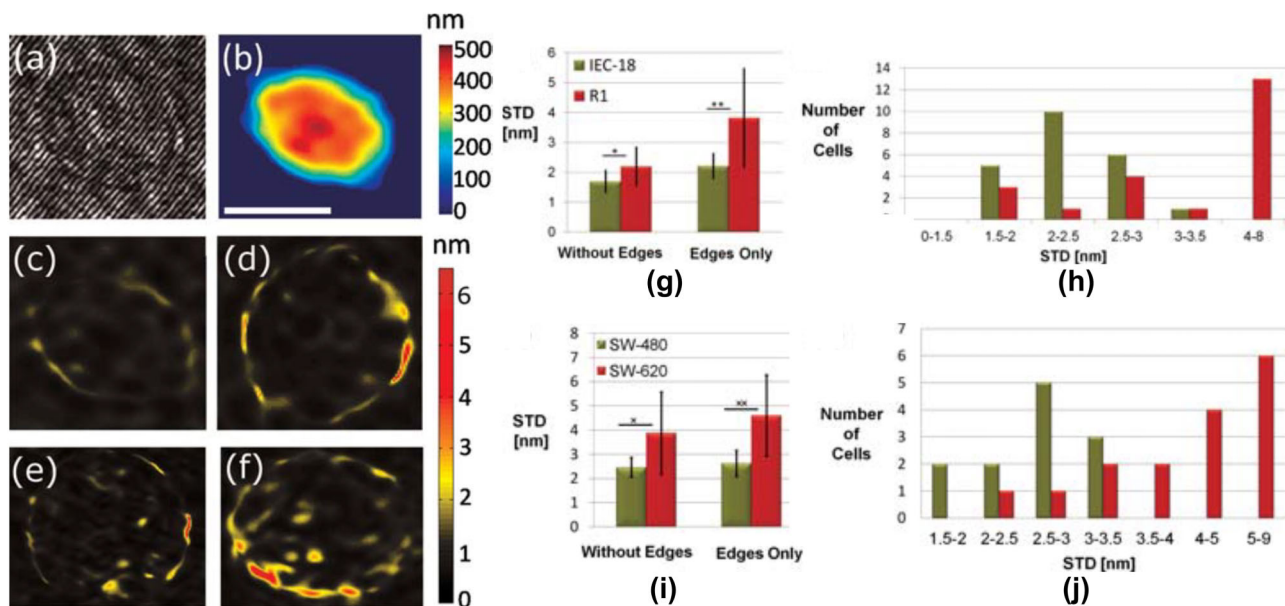


Figure 16 (a) Raw interferogram for a normal rat intestinal epithelial cell (IEC-18) acquired using IPM (b) Optical path-length map of the same cell. (c) and (d) Standard deviation (STD) of optical path-length in time for normal (IEC-18) and cancerous (R1) rat intestinal epithelial cells, respectively. (e) and (f) STD of optical path-length in time for primary (SW-480) and metastatic (SW-620) human colorectal carcinoma cells, respectively. (g) Results from analysis on rat intestinal epithelial cells. The maximum STD at both the edges of the cell and inside the rest of the cell were computed in each case. Bar heights show an average over 22 normal (IEC-18) and 22 cancerous (R1) cells. * refers to $p < 0.0025$ and ** refers to $p < 0.001$ based on the standard two-tailed unpaired t -test. (h) Histograms of the maximum STD for IEC-18 (green) and R1 (red) rat intestinal epithelial cells taken from the entire cell area (both edges and inside of the cell). (i) Results from analysis on primary (SW-480) and metastatic (SW-620) human colorectal carcinoma cells. The maximum STD at both the edges of the cell and inside the rest of the cell were computed in each case. Bar heights show an average over 12 primary cancer and 16 metastatic cells. * refers to $p < 0.005$ and ** refers to $p < 0.0003$ based on the standard two-tailed unpaired t -test. (j) Histogram of the maximum STD for SW-480 (green) and SW-620 (red) human colorectal carcinoma cells taken from the entire cell area (both edges and inside of the cell). Adapted with permission from Ref. [103].

Figure 16. As shown by the plots in Figure 16g–j, the maximum value of the STD in a cell at an advanced of the disease was on average higher and this difference was statistically significant. As discussed in Section 3.3.4, the temporal STD of optical path-length is inversely proportional to the stiffness of the cell membrane. This study points towards a possible marker for cancer that is based on cell stiffness and QPI techniques provide the means of extracting this marker in a convenient, non-contact and label-free manner. This study also shows that QPI can be a valuable tool to assist with liquid biopsy assessment, in addition to its utility in FFPE tissue-section based pathology.

4.5 Cancer diagnosis using photo-thermal phase microscopy

One of the common features of the diagnostic techniques discussed in this review is non-specificity to cell types. However, in conjunction with antibodies, QPI can be used to target cells expressing specific

antigens which can then be thermally ablated for therapeutic purposes, as demonstrated in Ref. [119]. In this work, the authors specifically targeted circulating tumor cells (CTC) in blood of cancer patients which can become seeds for distant metastasis in healthy organs. The targeted CTC cells expressed the epidermal growth factor receptor (and were thus called EGFR⁺). These cells were labelled with gold nanoparticles that were functionalized to attach to EGFRs. A modified version of IPM was used in this study, as is illustrated in Figure 17a. This setup uses two laser light sources: one serving as a source for phase imaging and the other as an excitation source for generating localized plasmons in the gold nanoparticles. The excitation source is operated in two modes: a low power mode for imaging and a high power mode for ablation. On excitation, the gold nanoparticles induce a change in phase in their vicinity due to release of thermal energy through excitation of localized plasmons. This phase change is referred to as the photothermal (PT) phase signal and is captured along with the regular phase image by the IPM, as described in the last section. The two signals are separated by modulating the excitation source

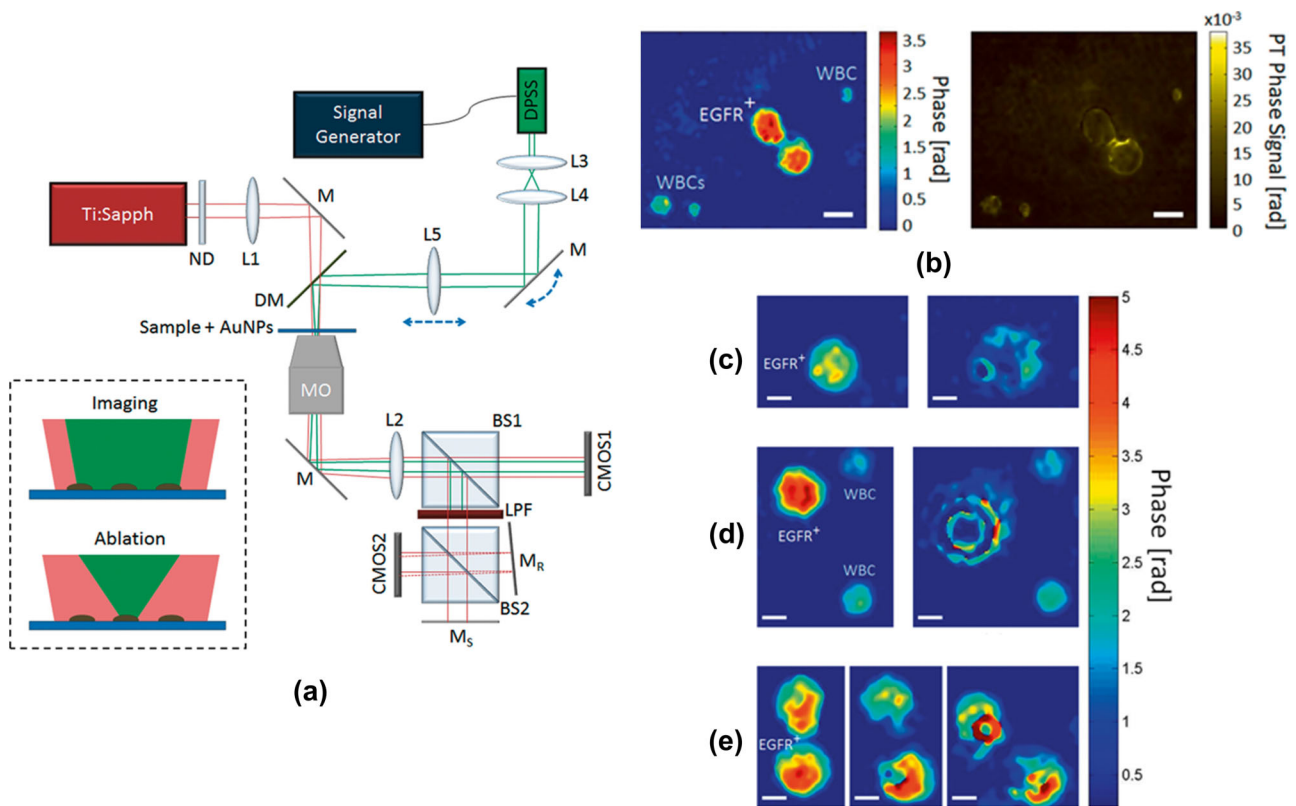


Figure 17 (a) Modified Interferometric Phase Microscopy (IPM) system for Photo-Thermal (PT) phase imaging. The diode-pumped solid-state laser (DPSS) is used for excitation of localized surface plasmons while the Titanium-Sapphire laser is used for the IPM based phase extraction. (b) PT phase imaging of MDA-MB-468 EGFR⁺ cells. The left image is a typical phase image obtained used IPM and shows both EGFR⁺ and EGFR⁻ (WBCs) cells. The PT Phase signal (right image), obtained in the low excitation power mode, on the other hand selectively shows EGFR⁺ cells. (c) A MDA-MB-468 EGFR⁺ cell before high-powered excitation (left) and after high powered excitation (right). (d) A MDA-MB-468 EGFR⁺ cell and WBCs before high-powered excitation (left) and after high powered excitation (right). (e) MDA-MB-468 EGFR⁺ cells before (left), during (middle) and after (right) high powered excitation. In each case (c–e) selective cell ablation is seen. Scale bars: 10 μm for (b) and 5 μm for (c–e). Adapted with permission from Ref. [119].

using a signal generator, which confines the PT signal to a frequency band, allowing its selective detection through band-pass filtering. Operating the excitation source in the high-power mode leads to release of enough thermal energy to cause cell ablation. Using such a technique provides the potential for simultaneous detection and treatment of target cancer cells at higher specificity than conventional QPI systems.

Figure 17 illustrates the images obtained using this method. The PT phase image, obtained in the low excitation power mode, only shows contrast in EGFR⁺ cells since the image contrast is generated by the presence of gold nanoparticles. As shown, operating the system in the high excitation power mode causes the selective ablation of EGFR⁺ cells.

4.6 Cancer diagnosis using FTLS

FTLS measurements (introduced in Section 3.3.5) have shown the ability to differentiate between different tissue types. Figure 18 demonstrates this ability for differentiating between rat brain, liver and kidney tissue. In this study Diffraction Phase Microscopy (DPM) was used to measure the complex image field and the scattering field was obtained by Fourier transforming the complex image field using Eq. (8). The three types of tissue show different values of scattering mean free path-length l_s , anisotropy factor g and transport mean free path $l^* = \frac{l_s}{1-g}$, as shown in Figure 18a–c. The values of l_s for this study were calculated from the phase maps using Lambert-Beer's law while the values of g were obtained by fitting the Gegenbauer–Kernel (G–K) equation to the scattering phase function versus scattering angle data, as shown in Figure 18d–f [120]. The scatter-

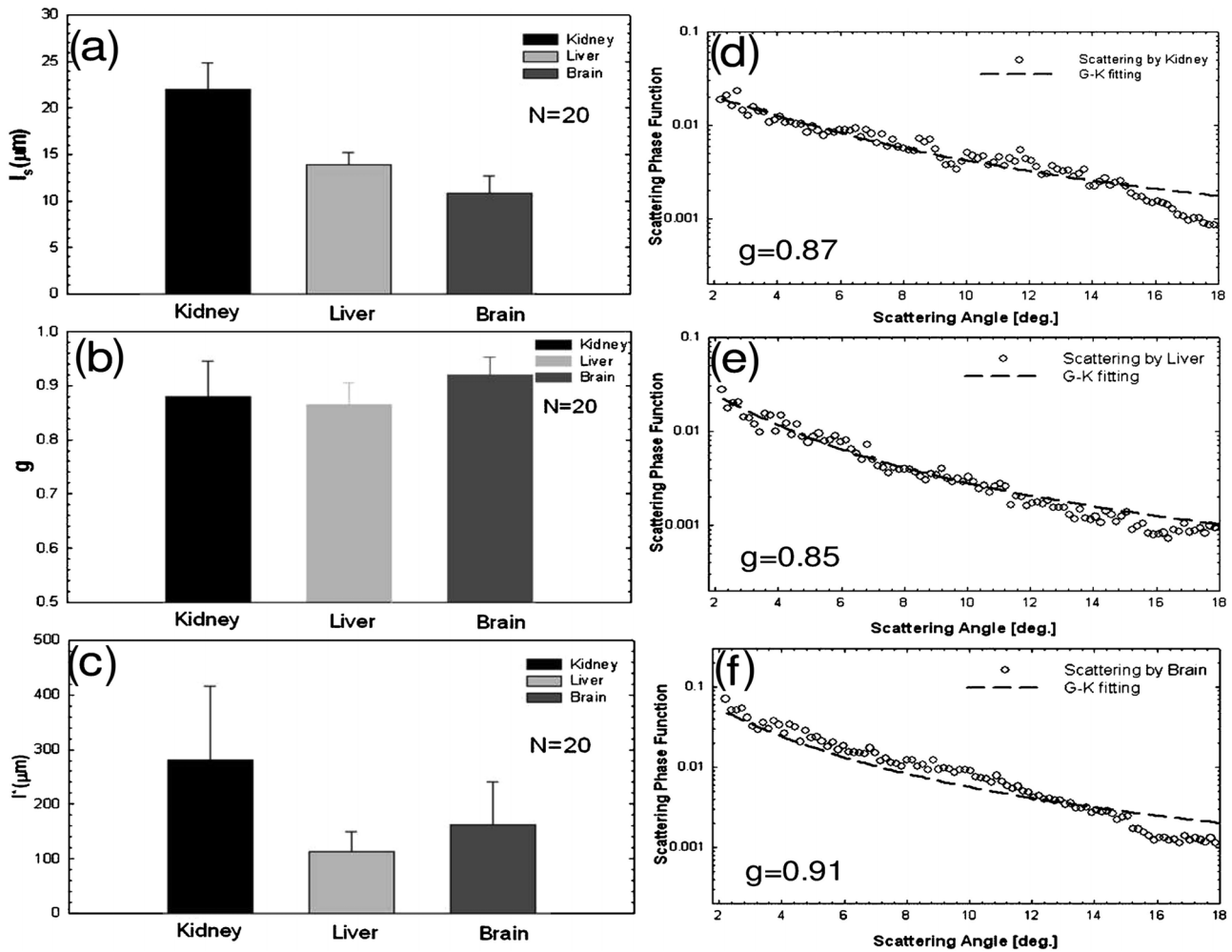


Figure 18 Comparison of (a) l_s , (b) g , (c) l^* for different types of mouse tissue. (d–f) Azimuthally averaged scattering field vs. scattering angle for kidney, liver and brain tissue. The value of g , obtained by fitting the data with the Gegenbauer-Kernel (GK) equation, is shown in each case. Adapted with permission from Ref. [120].

ing phase function versus scattering angle data was generated by taking the azimuthal average of the scattering field map $U(\mathbf{k})$ Eq. (8). While these results showed the ability of FTLS to separate tissues from different organs, to our knowledge a similar analysis has not been used to diagnose disease by comparing healthy versus diseased tissue. This may be a future avenue of exploration particularly when it comes to separating malignant from benign tissue in cancers.

4.7 Prostate cancer recurrence prediction using scattering anisotropy

The specific treatment administered to a cancer patient is determined by his or her prognosis. One of the key questions guiding advanced treatment options for prostate cancer patients who have under-

gone radical prostatectomy is whether they will have recurrence of disease at some point during their lifetime [121, 122]. As detailed in Ref. [99], a QPI method has shown the ability to predict recurrence by separating patients known to have cancer recurrence within 5 years post-prostatectomy from their matched twins who did not have recurrence. The pair were matched in terms of their age at prostatectomy, Gleason score (a standard prognostic tool) and disease stage [123]. Tissue microarrays obtained from this cohort were imaged using SLIM. The anisotropy parameter g (Section 4.3) was computed for the thin layer of stroma immediately adjoining the glands using the phase maps generated by SLIM. In total, this parameter was computed for 89 patients without recurrence, 89 matched cases with recurrence and 3 unmatched cases with recurrence. As shown in Figure 19, the values of anisotropy for the gland-adjacent stroma was higher in non-recurrent patients compared with recurrent patients. This

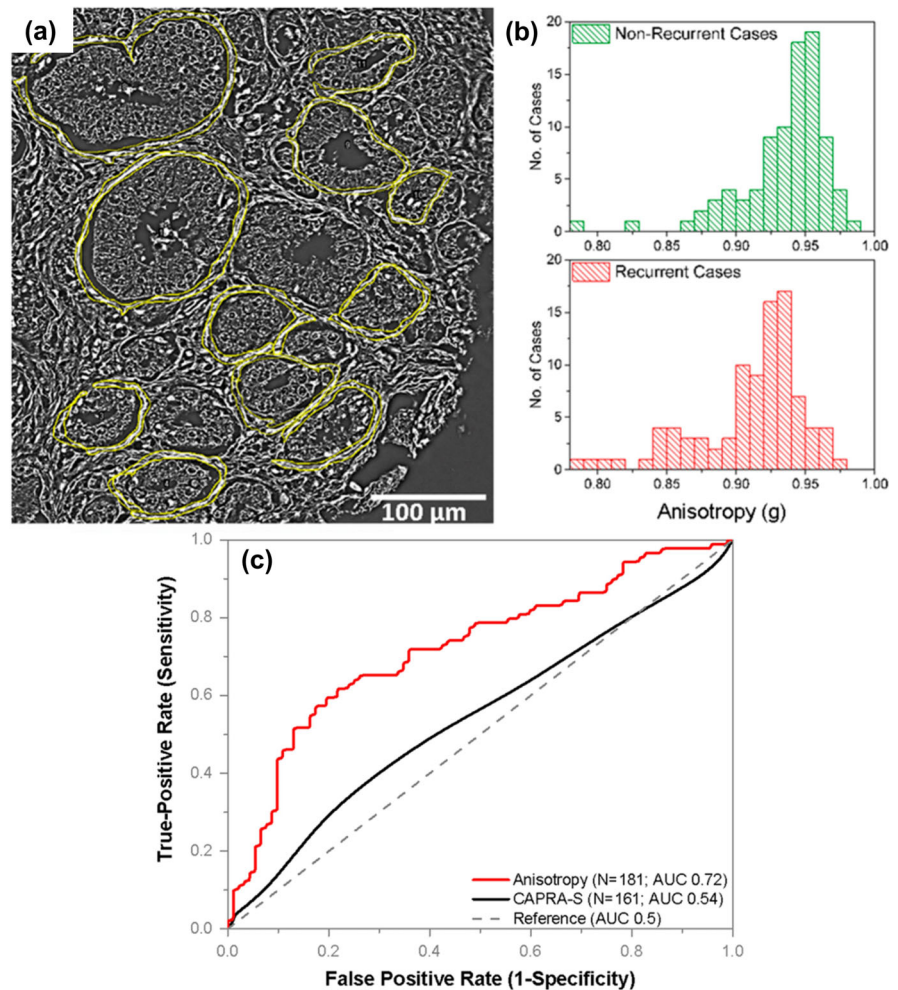


Figure 19 (a) SLIM image of prostate cancer tissue with thin layer of stroma, over which anisotropy g is calculated, marked out (b) Histograms of average g values for 89 Non-Recurrent and 92 Recurrent cases (c) Comparison of ROC curves for anisotropy and CAPRA-S, showing higher sensitivity and specificity for anisotropy. Adapted with permission from Ref. [99].

showed that the tumor adjacent stroma in patients at risk of recurrence was more fractionated, leading to scattering at higher angles on average. The area under the curve (AUC) value obtained from the receiver operating characteristic (ROC) curve was calculated as 0.72 using the anisotropy marker whereas the same using the clinical gold-standard prognostic tool Cancer of the Prostate Risk Assessment (CAPRA-S) score was significantly lower at 0.54 for a similar size of the cohort (Figure 19c). By relying on a label-free, quantitative parameter as the basis for prediction, this method provides a promising avenue for a rapid and accurate assessment of disease progression, to effectively inform treatment decisions.

4.8 Histopathology of Breast Cancer using QPI

Breast cancer is the second most common form of cancer diagnosed world-wide and accounted for 11.9% of all cancers diagnosed in 2012, according to

the WHO [125]. Due to wide prevalence and high mortality rate, breast cancer is often the subject of studies using quantitative imaging methods for disease diagnosis [100, 126–128]. Naturally, QPI methods have also been applied with the aim of improving the throughput and accuracy of breast cancer diagnosis. In the preliminary study reported in Ref. [124], the resolution and contrast of phase maps of breast cancer, generated using SLIM, were investigated by two board certified pathologists. The pathologists were first trained in interpreting cellular morphology from SLIM phase maps by showing them phase maps of 20 cores (out a total cohort of 109 cores) side by side with corresponding H&E stained tissue images. After this training procedure, the phase maps of the entire cohort were shown to the pathologists and they classified each core as either benign or malignant. Following this, the corresponding H&E stained tissue images were shown for the cohort and the pathologists marked their diagnosis on these images. The diagnosis of each pathologist on the H&E stained tissue was regarded as the gold standard and the number of agreements be-

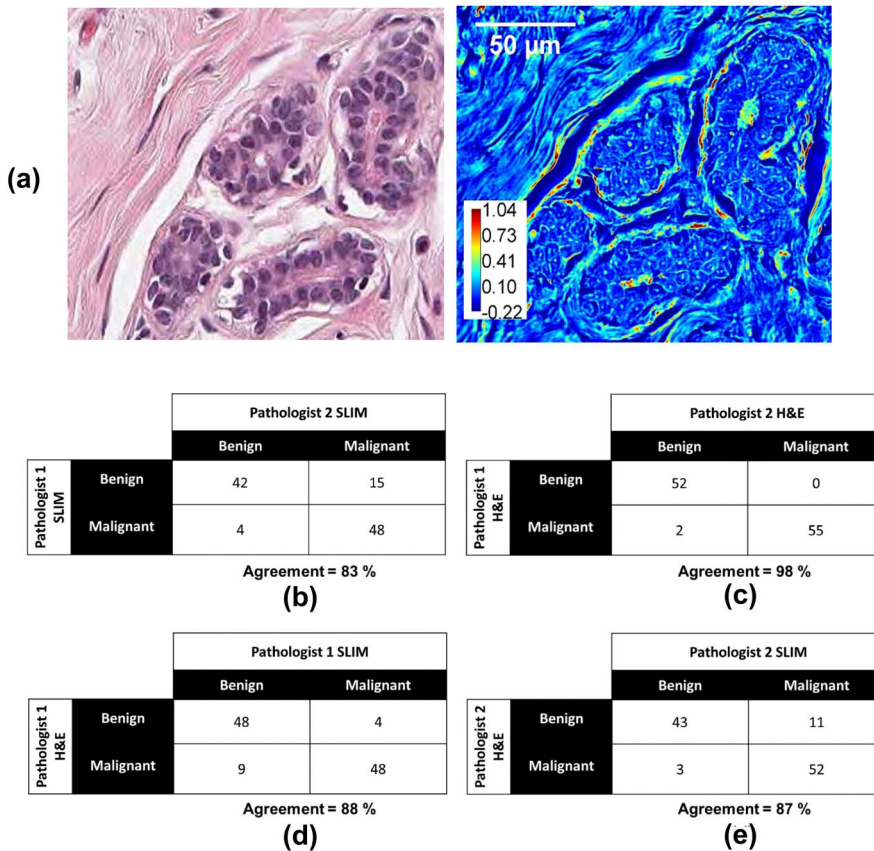


Figure 20 (a) Comparison of tissue morphological features as revealed by H&E (left) and SLIM (right). Color bar is in radians. (b–e) Confusion matrices summarizing the agreement between diagnoses of two board certified pathologists on SLIM and H&E. Adapted with permission from Ref. [124].

tween SLIM and H&E diagnoses were counted to measure the success of SLIM. The results are illustrated in Figure 20. The agreement between SLIM and H&E for pathologist 1 was 88% were as the same for pathologist 2 was 87%. The agreement between the diagnoses of the two pathologists using H&E (98%) was higher than the agreement using SLIM (83%). This discrepancy can be attributed to the fact that pathologists are trained for a number of years in interpreting cellular morphology from H&E stained tissue where as they had been trained in interpreting the same from SLIM phase maps for only 15–20 minutes. The study showed the promise QPI has, in its ability to capture morphological abnormalities, as a method for breast cancer diagnosis.

Another important problem related to breast cancer screening is that of detecting micro-calcifications in breast tissue during histological analysis. Micro-calcifications are generally detected during routine mammography and are considered an abnormality that may indicate early or pre-cancerous tissue [129]. If calcifications are found during mammography, the patient undergoes a biopsy and the tissue is forwarded to a pathologist for microscopic examination. Two types of micro-calcifications are typically found: calcium oxalate which are indicative of benign tissue and calcium phosphate which are indicative of pre-cancerous condition and are associated

with an increased risk of a cancer diagnosis in the future [130, 131]. It is important to be able to identify both of these crystals during histological examination due their clinical significance. However, the conventional H&E stain that is used to look at all other abnormalities generally does not stain calcium oxalate crystals. In order for the pathologist to detect these crystals, they have to switch to a polarization microscopy set-up. It was shown in Ref. [107] that SLIM is able to show the presence of calcium oxalate in addition to all the other morphological abnormalities (including calcium phosphate crystals) that mark disease (Figure 21). This illustrates an important advantage of QPI techniques in that they are able to provide all relevant morphological information in a single image that is not easily accessible with conventional microscopy.

4.9 Profilometry of pancreatic tumor cells

Figure 22 illustrates a study carried out using Digital Holographic Microscopy (DHM) on live human pancreatic tumor cells (optical setup illustrated in Figure 22a). The system employs laser-based off-axis interferometry in the Mach-Zehnder configuration. As shown, an interferogram is formed by the interfer-

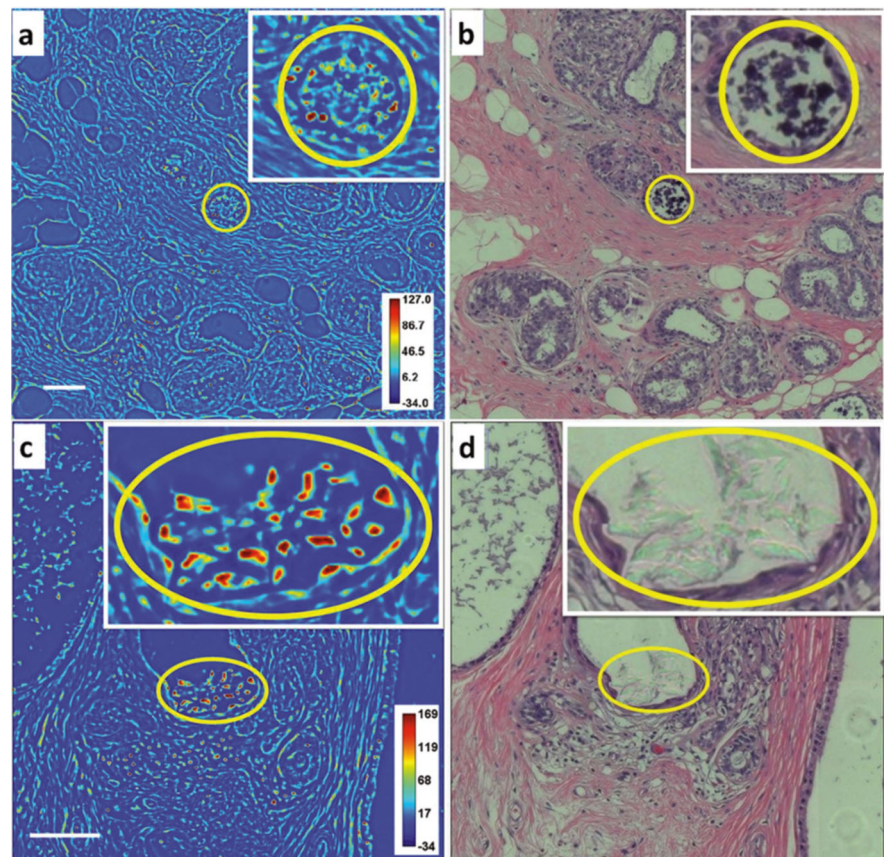


Figure 21 SLIM (left column) and H&E (right column) in their abilities to resolve (a–b) calcium phosphate (c–d) calcium oxalate microcalcifications. As shown, SLIM image are able to resolve both types of crystals while H&E staining only shows calcium phosphate crystals. Adapted with permission from Ref. [107].

ence of sample and reference waves at the CCD camera plane, from which the phase image can be extracted by using standard off-axis reconstruction, outlined in Section 1 of Supporting Information section [17]. In this study, the authors imaged cells with different metastatic potentials: poorly differentiated PaTu 8988T cells with high metastatic potential and low expression of E-Cadherin and PaTu 8988T p-LXIN E-Cadherin cells with lower metastatic potential due to higher expression of E-Cadherin caused by the transfection of p-LXIN vector containing DNA coding for E-Cadherin. The authors used DHM phase images to extract thickness maps and compared them for the two types of cells. The thickness maps were extracted from the phase images of the cells by assuming a uniform, constant refractive index for the cells. This cell refractive index was measured by deforming the cell until it had uniform constant thickness, taking the phase image of this deformed cell and extracting the cell refractive index from the phase image by using Eq. (5). As shown in Figure 22, the thickness profiles for cells showing greater expression of the tumor suppressor E-Cadherin were markedly different from those of cells with under-expression of the protein. Such analyses can be used to detect and investigate tumor progression in pancreatic cells in a label-free, quantitative and non-contact manner [102].

5. Summary and discussion

Without a doubt, Quantitative Phase Imaging (QPI) has turned the corner from an instrument development to an application driven field. This transition is due in great part to the technological progress that resulted in reliable QPI instruments, of high stability and sensitivity, which can now deliver repeatable results. While so far most applications have revolved around live cell imaging, it is clear that QPI holds huge potential for clinical applications. The label-free operation and quantitative data associated with QPI are likely to offer a new avenue for high-throughput, objective diagnosis for a number of diseases.

Light scattering techniques have established decades ago the relationship between cancer onset and development and tissue refractive index modifications. Today, QPI can measure precisely these changes in refractive index that accompany disease states. A quantitative phase image of an unlabeled biopsy also reveals the complexity of the problem: tissue refractive index is highly inhomogeneous, it varies greatly across an organ and from organ to organ.

Expressions such as “the refractive index of liver is ...” does not carry any significant meaning. The

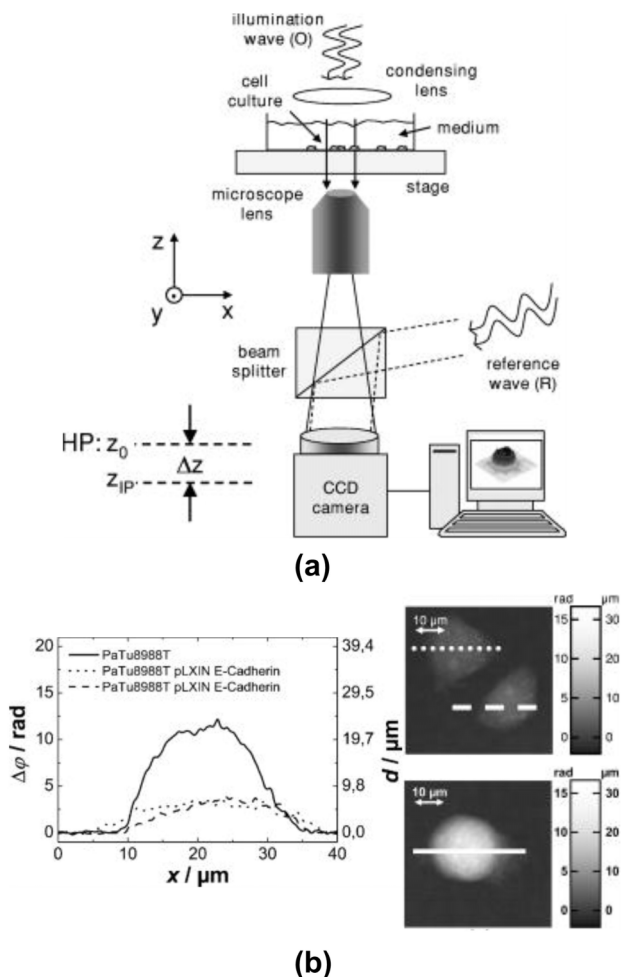


Figure 22 (a) Optical setup of Digital Holographic Microscopy (DHM) used in this study. (b) Thickness profiles of cells with different metastatic potentials (left), along cross-sections shown on the images (right). Adapted with permission from Ref. [102].

refractive index is a statistical quantity that is best described through moments (mean, variance, etc.) and spatial correlations. Despite the complexity of this problem, preliminary results have already demonstrated the capability of QPI for not only diagnosis, but also prognosis in cancer pathology. The label-free operation means that the information is not biased by the staining procedure. The lack of staining also cuts down the time and expense of the biopsy preparations. Perhaps more importantly, the phase map is an objective representation of the specimen, meaning that multiple measurements can be compared without the need for calibration, color correction etc. This feature is crucial in developing computational algorithms for automatic diagnosis. Machine learning algorithms will become more performant as the data pool available for training increases. For this reason alone, it is important that the QPI community works together, shares data and

perhaps contributes toward a unified cloud-based data repository.

Contributing to the tremendous excitement surrounding the QPI field, we note that today there are approximately a dozen start-up companies operating in the QPI space. As the technology moves its way into the hands of the biomedical researchers, we anticipate that studies of longer depth, of higher impact will soon emerge. We will witness discoveries in areas that, to date, have been unaddressed.

Supporting Information

Additional supporting information can be found in the online version of this article at the publisher's website.

Acknowledgements This work is supported by Phi Optics Inc., the National Science Foundation (NSF) through the Science & Technology Center on Emergent Behaviors of Integrated Cellular Systems CBET 0939511 and Future-leading Specialized Research Fund (1.160060.01) of UNIST (Ulsan National Institute of Science and Technology), South Korea.

Conflict of Interest Dr. Popescu has financial interest in Phi Optics Inc., a company that commercializes quantitative phase imaging instruments and is one of the sponsors of the work.

Author biographic Please see Supporting Information online.

References

- [1] M. Born and E. Wolf, *Principles of Optics: Electromagnetic Theory of Propagation, Interference and Diffraction of Light*, Pergamon Press, New York, 1964.
- [2] G. Popescu, *Quantitative Phase Imaging of Cells and Tissues*, McGraw Hill, 2011.
- [3] Y. Park, M. Diez-Silva, G. Popescu, G. Lykotrafitis, W. Choi, M. S. Feld, and S. Suresh, *Proceedings of the National Academy of Sciences*. **105**, 13730–13735 (2008).
- [4] Y. Park, C. A. Best, K. Badizadegan, R. R. Dasari, M. S. Feld, T. Kuriabova, M. L. Henle, A. J. Levine, and G. Popescu, *Proceedings of the National Academy of Sciences*. **107**, 6731–6736 (2010).
- [5] Y. Park, C. A. Best, T. Auth, N. S. Gov, S. A. Safran, G. Popescu, S. Suresh, and M. S. Feld, *Proceedings of the National Academy of Sciences*. **107**, 1289–1294 (2010).
- [6] G. Popescu, Y. Park, N. Lue, C. Best-Popescu, L. Deflores, R. R. Dasari, M. S. Feld, and K. Badizadegan, *American Journal of Physiology – Cell Physiology*. **295**, C538–C544 (2008).

- [7] M. Mir, Z. Wang, Z. Shen, M. Bednarz, R. Bashir, I. Golding, S. G. Prasanth, and G. Popescu, *Proceedings of the National Academy of Sciences*. **108**, 13124–13129 (2011).
- [8] K. L. Cooper, S. Oh, Y. Sung, R. R. Dasari, M. W. Kirschner, and C. J. Tabin, *Nature*. **495**, 375–378 (2013).
- [9] H. Ding, Z. Wang, F. T. Nguyen, S. A. Boppart, L. J. Millet, M. U. Gillette, J. Liu, M. D. Boppart, and G. Popescu, *Journal of Computational and Theoretical Nanoscience*. **7**, 2501–2511 (2010).
- [10] Y. Kim, H. Shim, K. Kim, H. Park, J. H. Heo, J. Yoon, C. Choi, S. Jang, and Y. Park, *Optics Express*. **22**, 10398–10407 (2014).
- [11] W. Choi, C. Fang-Yen, K. Badizadegan, S. Oh, N. Lue, R. R. Dasari, and M. S. Feld, *Nat Meth*. **4**, 717–719 (2007).
- [12] T. Kim, R. Zhou, M. Mir, S. D. Babacan, P. S. Carney, L. L. Goddard, and G. Popescu, *Nat Photon*. **8**, 256–263 (2014).
- [13] M. Lee, E. Lee, J. Jung, H. Yu, K. Kim, S. Lee, Y. Jeong, and Y. Park, arXiv preprint arXiv:1603.00698. 2016.
- [14] I. Crha, J. Zakova, M. Huser, P. Ventruba, E. Lousova, and M. Pohanka, *Journal of Assisted Reproduction and Genetics*. **28**, 725–729 (2011).
- [15] B. Kemper, Á. Barroso, M. Woerdemann, L. Dewenter, A. Vollmer, R. Schubert, A. Mellmann, G. von Bally, and C. Denz, *Journal of Biophotonics*. **6**, 260–266 (2013).
- [16] H. V. Pham, L. Pantanowitz, and Y. Liu, *Cancer Cytopathology*. 2016, n/a-n/a.
- [17] H. Majeed, S. Sridharan, M. Mir, L. Ma, E. Min, W. Jung, and G. Popescu, *Journal of Biophotonics: Supporting Information*, S1–S5 (2016).
- [18] R. Barer *Nature*. **169**, 366–367 (1952).
- [19] H. G. Davies and M. H. Wilkins, *Nature*. **169**, 541 (1952).
- [20] B. Rappaz, A. Barbul, Y. Emery, R. Korenstein, C. Depeursinge, P. J. Magistretti, and P. Marquet, *Cytometry Part A*. **73A**, 895–903 (2008).
- [21] R. Wang, Z. Wang, L. Millet, M. U. Gillette, A. Levine, and G. Popescu, *Optics Express* **19**, 20571–20579 (2011).
- [22] B. Rappaz, F. Charrière, C. Depeursinge, P. J. Magistretti, and P. Marquet, *Optics Letters*. **33**, 744–746 (2008).
- [23] P. Sarder and A. Nehorai, *IEEE Signal Processing Magazine*. **23**, 32–45 (2006).
- [24] B. J. Bain, *Blood cells: a practical guide*, John Wiley & Sons, 2014.
- [25] E. J. Corwin, L. Williams, *The Hematologic System in Handbook of Pathophysiology*, Lippincott Williams & Wilkins Philadelphia, 2000.
- [26] B. J. Bain, *New England Journal of Medicine*. **353**, 498–507 (2005).
- [27] D. H. Ryan, Chapter 2. Examination of Blood Cells in *Williams Hematology*, 8e (Eds.: M. A. Lichtman, T. J. Kipps, U. Seligsohn, K. Kaushansky, J. T. Prchal), The McGraw-Hill Companies, New York, NY, 2010.
- [28] *Fact Book Fiscal Year 2012*, National Heart, Lung, and Blood Institute; U.S Department of Health and Human Services, 2013.
- [29] J. Ojodu, M. M. Hulihan, S. N. Pope, and A. M. Grant, *MMWR Morb Mortal Wkly Rep*. **63**, 1155–1158 (2014).
- [30] Global Health Observatory (GHO) data: Malaria, World Health Organization (2005), <http://www.who.int/gho/malaria/en/>
- [31] P. Peterson, S. McNeill, G. Gulati, *Cellular Morphologic Analysis of Peripheral Blood in Laboratory Hematology Practice*, Wiley-Blackwell, 2012, pp. 10–25.
- [32] G. M. Davis, K. L. Lantis, W. G. Finn, *Laboratory Hematology Practice in Hematopathology in Oncology*, Springer 2004, pp. 167–179.
- [33] R. V. Pierre, *Clinics in Laboratory Medicine*. **22**, 279–297 (2002).
- [34] M. Mir, K. Tangella, and G. Popescu, *Biomedical Optics Express*. **2**, 3259–3266 (2011).
- [35] I. Moon, B. Javidi, F. Yi, D. Boss, and P. Marquet, *Optics Express*. **20**, 10295–10309 (2012).
- [36] G. Popescu, T. Ikeda, C. A. Best, K. Badizadegan, R. R. Dasari, and M. S. Feld, *Journal of Biomedical Optics*. **10**, 060503 (2005).
- [37] H. V. Pham, B. Bhaduri, K. Tangella, C. Best-Popescu, and G. Popescu, *PLoS One*. **8**, e55676 (2013).
- [38] M. Aikawa, *Biology of the Cell*. **64**, 173–181 (1988).
- [39] M. Kruatrachue and S. Na-Nakorn, *Bulletin of the World Health Organization*. **47**, 665–669 (1972).
- [40] L. W. Diggs and J. Bibb, *Journal of the American Medical Association*. **112**, 695–701 (1939).
- [41] K. Kim, H. Yoon, M. Diez-Silva, M. Dao, R. R. Dasari, and Y. Park, *Journal of Biomedical Optics*. **19**, 011005 (2013).
- [42] M. Mir, H. Ding, Z. Wang, J. Reedy, K. Tangella, and G. Popescu, *Journal of Biomedical Optics*. **15**, 027016 (2010).
- [43] M. Mir, Z. Wang, K. Tangella, and G. Popescu, *Optics Express*. **17**, 2579–2585 (2009).
- [44] Y. Kim, H. Shim, K. Kim, H. Park, S. Jang, and Y. Park, *Scientific Reports*. **4**, 6659 (2014).
- [45] G. Popescu, T. Ikeda, R. R. Dasari, and M. S. Feld, *Optics letters*. **31**, 775–777 (2006).
- [46] B. Bhaduri, C. Edwards, H. Pham, R. Zhou, T. H. Nguyen, L. L. Goddard, and G. Popescu, *Adv. Opt. Photon*. **6**, 57–119 (2014).
- [47] V. Lauer, *Journal of Microscopy*. **205**, 165–176 (2002).
- [48] K. Kim, K. S. Kim, H. Park, J. C. Ye, and Y. Park, *Optics Express*. **21**, 32269–32278 (2013).
- [49] H. Park, S.-H. Hong, K. Kim, S.-H. Cho, W.-J. Lee, Y. Kim, S.-E. Lee, and Y. Park, *Scientific Reports*. **5**, 10827 (2015).
- [50] P. Memmolo, L. Miccio, F. Merola, O. Gennari, P. A. Netti, and P. Ferraro, *Cytometry Part A*. **85**, 1030–1036 (2014).
- [51] N. Cardenas and S. K. Mohanty, *Applied Physics Letters*. **103**, 013703 (2013).
- [52] F. Merola, L. Miccio, P. Memmolo, G. Di Caprio, A. Galli, R. Puglisi, D. Balduzzi, G. Coppola, P. Netti, and P. Ferraro, *Lab on a Chip*. **13**, 4512–4516 (2013).

- [53] J. Jung, L. E. Matemba, K. Lee, P. E. Kazyoba, J. Yoon, J. J. Massaga, K. Kim, D.-J. Kim, and Y. Park, arXiv preprint arXiv:1604.06796. 2016.
- [54] H. Park, T. Ahn, K. Kim, S. Lee, S.-y. Kook, D. Lee, I. B. Suh, S. Na, and Y. Park, *Journal of Biomedical Optics*. **20**, 111208–111208 (2015).
- [55] I. Moon, F. Yi, Y. H. Lee, B. Javidi, D. Boss, and P. Marquet, *Optics Express*. **21**, 30947–30957 (2013).
- [56] H. Park, M. Ji, S. Lee, K. Kim, Y.-H. Sohn, S. Jang, and Y. Park, arXiv preprint arXiv:1506.05259. 2015.
- [57] B. Rappaz, P. Marquet, E. Cuche, Y. Emery, C. Depeursinge, and P. Magistretti, *Optics Express*. **13**, 9361–9373 (2005).
- [58] Y. Jang, J. Jang, and Y. Park, *Optics Express*. **20**, 9673–9681 (2012).
- [59] M. T. Rinehart, H. S. Park, K. A. Walzer, J.-T. A. Chi, and A. Wax, *Scientific Reports*. **6**, 24461 (2016).
- [60] H. Byun, T. R. Hillman, J. M. Higgins, M. Diez-Silva, Z. Peng, M. Dao, R. R. Dasari, S. Suresh, and Y. Park, *Acta Biomaterialia*. **8**, 4130–4138 (2012).
- [61] S. Chien, *Annual Review of Physiology*. **49**, 177–192 (1987).
- [62] J. M. Sosa, N. D. Nielsen, S. M. Vignes, T. G. Chen, and S. S. Shevkopyas, *Clinical Hemorheology and Microcirculation*. **57**, 291–305 (2014).
- [63] H. Reid, A. Barnes, P. Lock, J. Dormandy, and T. Dormandy, *Journal of Clinical Pathology*. **29**, 855–858 (1976).
- [64] N. Mohandas and P. G. Gallagher, *Blood*. **112**, 3939–3948 (2008).
- [65] N. Gov and S. A. Safran, *Journal of Biological Physics*. **31**, 453–464 (2005).
- [66] N. Gov, A. G. Zilman, and S. Safran, *Physical Review Letters*. **90**, 228101 (2003).
- [67] Y. Park, C. Best, and G. Popescu, *Optical Sensing of Red Blood Cell Dynamics in Mechanobiology of Cell-Cell and Cell-Matrix Interactions*, (Eds.: A. Wagoner Johnson, B. A. C. Harley), Springer US, 2011, pp. 279–309.
- [68] I. Shock, A. Barbul, P. Girshovitz, U. Nevo, R. Korenstein, and N. T. Shaked, *Journal of Biomedical Optics*. **17**, 1015091–1015095 (2012).
- [69] N. T. Shaked, L. L. Satterwhite, M. J. Telen, G. A. Truskey, and A. Wax, *Journal of Biomedical Optics*. **16**, 030506 (2011).
- [70] N. T. Shaked, L. L. Satterwhite, N. Bursac, and A. Wax, *Biomedical Optics Express*. **1**, 706–719 (2010).
- [71] B. Bhaduri, M. Kandel, C. Brugnara, K. Tangella, and G. Popescu, *Scientific Reports*. **4**, 6211 (2014).
- [72] Z. Wang, L. Millet, M. Mir, H. Ding, S. Unarunotai, J. Rogers, M. U. Gillette, and G. Popescu, *Optics Express*. **19**, 1016–1026 (2011).
- [73] V. Backman, V. Gopal, M. Kalashnikov, K. Badizadegan, R. Gurjar, A. Wax, I. Georgakoudi, M. Mueller, C. W. Boone, R. R. Dasari, and M. S. Feld, *IEEE Journal of Selected Topics in Quantum Electronics*. **7**, 887–893 (2001).
- [74] R. M. Doornbos, M. Schaeffer, A. G. Hoekstra, P. M. Sloot, B. G. Grooth, and J. Greve, *Applied Optics*. **35**, 729–734 (1996).
- [75] H. Ding, Z. Wang, F. Nguyen, S. A. Boppart, and G. Popescu, *Physical Review Letters*. **101**, 238102 (2008).
- [76] Y. Jo, J. Jung, J. W. Lee, D. Shin, H. Park, K. T. Nam, J.-H. Park, and Y. Park, *Scientific Reports*. **4**, 5090 (2014).
- [77] K. Kim and Y. Park *Optics Letters*. **37**, 4161–4163 (2012).
- [78] K. Lee, H.-D. Kim, K. Kim, Y. Kim, T. R. Hillman, B. Min, and Y. Park, *Optics Express*. **21**, 22453–22463 (2013).
- [79] Y. Kim, J. M. Higgins, R. R. Dasari, S. Suresh, and Y. Park, *Journal of Biomedical Optics*. **17**, 040501 (2012).
- [80] Y. K. Park, G. Popescu, K. Badizadegan, R. R. Dasari, and M. S. Feld, *Optics Express*. **14**, 8263–8268 (2006).
- [81] T. A. Zangle, D. Burnes, C. Mathis, O. N. Witte, and M. A. Teitell, *PLoS ONE*. **8**, e68916 (2013).
- [82] K. J. Chalut, A. E. Ekpenyong, W. L. Clegg, I. C. Melhuish, and J. Guck, *Integrative Biology*. **4**, 280–284 (2012).
- [83] S. Lee, Y. R. Kim, J. Y. Lee, J. H. Rhee, C.-S. Park, and D. Y. Kim, *Journal of Biomedical Optics*. **16**, 036004–036007 (2011).
- [84] J. Yoon, K. Kim, H. Park, C. Choi, S. Jang, and Y. Park, *Biomedical Optics Express*. **6**, 3865–3875 (2015).
- [85] A. E. Ekpenyong, S. M. Man, S. Achouri, C. E. Bryant, J. Guck, and K. J. Chalut, *Journal of Biophotonics*. **6**, 393–397 (2013).
- [86] E. Cuche, F. Bevilacqua, and C. Depeursinge, *Optics Letters*. **24**, 291–293 (1999).
- [87] E. Cuche, P. Marquet, and C. Depeursinge, *Applied Optics*. **38**, 6994–7001 (1999).
- [88] M. K. Kim, *Digital Holographic Microscopy in Digital Holographic Microscopy: Principles, Techniques, and Applications*, Springer New York, New York, NY, 2011, pp. 149–190.
- [89] Cancer: Fact Sheet, World Health Organization, 2013. URL: <http://www.who.int/mediacentre/factsheets/fs297/en/>
- [90] Estimates of Funding for Various Research, Condition, and Disease Categories (RCDC), National Institute of Health, (2015). http://report.nih.gov/categorical_spending.aspx
- [91] A. H. Fischer, K. A. Jacobson, J. Rose, and R. Zeller, *CSH Protoc.*, pdb prot4986 (2008).
- [92] N. Wissozky, *Archiv für mikroskopische Anatomie*. **13**, 479–496 (1877).
- [93] R. Rickert and R. Maliniak, *Archives of Pathology & Laboratory Medicine*. **113**, 673–679 (1989).
- [94] M. Miettinen *APMIS*. **98**, 191–199 (1990).
- [95] L. L. de Matos, D. C. Trufelli, M. G. L. de Matos, and M. A. da Silva Pinhal, *Biomarker Insights*. **5**, 9–20 (2010).
- [96] M. R. Wick, *Ann Diagn Pathol*. **12**, 72–84 (2008).
- [97] T. Seidal, A. J. Balaton, and H. Battifora, *The American Journal of Surgical Pathology*. **25**, 1204–1207 (2001).
- [98] C. R. Taylor and R. M. Levenson, *Histopathology*. **49**, 411–424 (2006).

- [99] S. Sridharan, V. Macias, K. Tangella, A. Kajdacsy-Balla, and G. Popescu, *Scientific Reports*. **5**, 9976 (2015).
- [100] M. W. Conklin, J. C. Eickhoff, K. M. Ricking, C. A. Pehlke, K. W. Eliceiri, P. P. Provenzano, A. Friedl, and P. J. Keely, *The American Journal of Pathology*. **178**, 1221–1232 (2011).
- [101] B. J. Vakoc, R. M. Lanning, J. A. Tyrrell, T. P. Padera, L. A. Bartlett, T. Stylianopoulos, L. L. Munn, G. J. Tearney, D. Fukumura, R. K. Jain, and B. E. Bouma, *Nat Med*. **15**, 1219–1223 (2009).
- [102] B. Kemper, D. Carl, J. Schneidenburger, I. Bredebusch, M. Schäfer, W. Domschke, and G. von Bally, *Journal of Biomedical Optics*. **11**, 034005–034008 (2006).
- [103] Y. Bishitz, H. Gabai, P. Girshovitz, and N. T. Shaked, *Journal of Biophotonics*. **7**, 624–630 (2014).
- [104] S. P. Langdon, *Cancer cell culture: methods and protocols*, Springer Science & Business Media, 2004.
- [105] E. Rosenthal and K. R. Zinn, *Optical imaging of cancer*, Springer, 2009.
- [106] Z. Wang, H. Ding, and G. Popescu, *Optics letters*. **36**, 1215–1217 (2011).
- [107] Z. Wang, G. Popescu, K. V. Tangella, and A. Balla, *Journal of Biomedical Optics*. **16**, 116017 (2011).
- [108] R. Horstmeyer, X. Ou, G. Zheng, P. Willems, and C. Yang, *Computerized Medical Imaging and Graphics*. **42**, 38–43 (2015).
- [109] N. Lue, J. Bewersdorf, M. D. Lessard, K. Badizadegan, R. R. Dasari, M. S. Feld, and G. Popescu, *Optics Letters*. **32**, 3522–3524 (2007).
- [110] T. Ikeda, G. Popescu, R. R. Dasari, and M. S. Feld, *Optics Letters*. **30**, 1165–1167 (2005).
- [111] P. Wang, R. K. Bista, W. E. Khalbuss, W. Qiu, S. Uttam, K. Staton, L. Zhang, T. A. Brentnall, R. E. Brand, and Y. Liu, *Journal of Biomedical Optics*. **15**, 066028 (2010).
- [112] P. Wang, R. Bista, R. Bhargava, R. E. Brand, and Y. Liu, *Optics Letters*. **35**, 2840–2842 (2010).
- [113] A. Wax, C. Yang, and J. A. Izatt, *Optics Letters*. **28**, 1230–1232 (2003).
- [114] S. Uttam, H. V. Pham, J. LaFace, B. Leibowitz, J. Yu, R. E. Brand, D. J. Hartman, and Y. Liu, *Cancer Research*. **75**, 4718–4727 (2015).
- [115] R. K. Bista, P. Wang, R. Bhargava, S. Uttam, D. J. Hartman, R. E. Brand, and Y. Liu, *Breast Cancer Research and Treatment*. **135**, 115–124 (2012).
- [116] A. M. Krasinskas, R. K. Bista, S. Rizvi, D. J. Hartman, M. Sanders, A. Gelrud, A. Slivka, R. Brand, and Y. Liu, *Gastroenterology* **140**, 68 (2011).
- [117] D. J. Hartman, A. M. Krasinskas, S. Uttam, K. Staton, R. Bista, S. Rizvi, A. Slivka, R. Brand, and Y. Liu, *Am J Clin Pathol*. **141**, 884–891 (2014).
- [118] D. A. Brokl, D. Y. Lo, W. E. Khalbuss, P. Wang, R. K. Bista, S. Uttam, Y. Liu, and R. Brand, *Gastroenterology*, **140**, 53 (2011).
- [119] N. A. Turko, I. Barnea, O. Blum, R. Korenstein, and N. T. Shaked, *Journal of Biophotonics*. **8**, 755–763 (2015).
- [120] H. Ding, F. Nguyen, S. A. Boppart, and G. Popescu, *Optics Letters*. **34**, 1372–1374 (2009).
- [121] S. E. Eggener, P. T. Scardino, P. C. Walsh, M. Han, A. W. Partin, B. J. Trock, Z. Feng, D. P. Wood, J. A. Eastham, O. Yossepowitch, D. M. Rabah, M. W. Kattan, C. Yu, E. A. Klein, and A. J. Stephenson, *The Journal of Urology*, **185**, 869–875 (2011).
- [122] G. W. Hull, F. Rabbani, F. Abbas, T. M. Wheeler, M. W. Kattan, and P. T. Scardino, *The Journal of Urology*, **167**, 528–534 (2002).
- [123] M. R. Cooperberg, J. F. Hilton, and P. R. Carroll, *Cancer*. **117**, 5039–5046 (2011).
- [124] H. Majeed, M. E. Kandel, K. Han, Z. Luo, V. Macias, K. Tangella, A. Balla, and G. Popescu, *Journal of Biomedical Optics*. **20**, 111210 (2015).
- [125] Latest world cancer statistics Global cancer burden rises to 14.1 million new cases in 2012: Marked increase in breast cancers must be addressed, World Health Organization, 2013. URL: http://www.iarc.fr/en/media-centre/pr/2013/pdfs/pr223_E.pdf.
- [126] A. Benard, C. Desmedt, M. Smolina, P. Szternfeld, M. Verdonck, G. Rouas, N. Kheddoumi, F. Rothe, D. Larsimont, C. Sotiriou, and E. Goormaghtigh, *Analyst*. **139**, 1044–1056 (2014).
- [127] M. J. Walsh, S. E. Holton, A. Kajdacsy-Balla, and R. Bhargava, *Vibrational Spectroscopy*. **60**, 23–28 (2012).
- [128] F. T. Nguyen, A. M. Zysk, E. J. Chaney, J. G. Kotynek, U. J. Oliphant, F. J. Bellafiore, K. M. Rowland, P. A. Johnson, and S. A. Boppart, *Cancer Research*. **69**, 8790–8796 (2009).
- [129] G. Tse, P. H. Tan, A. L. Pang, A. P. Tang, and H. S. Cheung, *Journal of Clinical Pathology*. **61**, 145–151 (2008).
- [130] M. J. Radi, *Archives of pathology & laboratory medicine*. **113**, 1367–1369 (1989).
- [131] J. S. Winston, I.-T. Yeh, K. Evers, and A. K. Friedman, *American Journal of Clinical Pathology*. **100**, 488–492 (1993).